

YTTERBIUM ION QUBIT STATE DETECTION ON AN ICCD CAMERA

by
Aaron Christopher Lee

A senior honors thesis submitted to the Department of Physics
of the University of Maryland, College Park in partial fulfillment
of the requirements for the degree of
Bachelor of Science in Physics
2012

Defense Committee:

Professor Christopher R. Monroe, Chair
Professor Richard F. Ellis
Professor Christopher Jarzynski
Professor Frederick Wellstood

“It’s still magic even if you know how it’s done.”
—Terry Pratchett

© Aaron Christopher Lee
All Rights Reserved
2012

To my wife, Ada, and our daughters, Aria and Alyssa.

ACKNOWLEDGEMENTS

I would like to thank my advisor, Chris Monroe, for giving me the opportunity to work with him as an undergraduate assistant. His support has enabled me to participate in phenomenal research and I cannot thank him enough.

I especially want to thank Wes Campbell, who has not only helped me on a daily basis, but who has also shown me what it means to be a physicist and how a physicist should view the world. I hope to live up to the example he has set me.

Additionally, I would also like to thank Rajibul Islam, Simcha Korenblit, Crystal Senko, and Jake Smith for always being willing to answer questions and help with problems. Without their assistance, I would not have been able to accomplish so much as an undergraduate.

I also want to thank everyone with whom I have worked in the lab. Everyone of you has helped me at some point or another. All of you have been a blast to work with. Thus, I would like to thank Susan Clark, Taeyoung Choi, Shantanu Debnath, Kale Johnson, Andrew Manning, Dave Hayes, Jonathan Mizrahi, David Hucul, Kenny Lee, Brian Fields, Daniel Brennan, Emily Edwards, Kihwan Kim, and Jon Sterk.

My friends I thank for always being supportive and helping me to keep a level head and a humble heart.

Most of all, I would like to thank the love of my life, Ada, who has been my greatest support. She has been a constant source of love and advice. She has also

been my font of perfect spelling and grammar. I would also like to thank my two beautiful little girls, Aria and Alyssa, who always put a smile on my face. To you, Ada, Aria, and Alyssa, I dedicate this thesis.

TABLE OF CONTENTS

DEDICATION	ii
ACKNOWLEDGEMENTS	iii
LIST OF TABLES	vi
LIST OF FIGURES	vii
ABSTRACT	ix
CHAPTER	
I. Introduction	1
II. Ytterbium Detection	3
2.1 The Detection Transition	3
2.2 Off-Resonant Coupling	4
2.3 Finding α_1 and α_2	8
2.4 Detection with the PMT	11
III. The ICCD Camera	14
3.1 Introduction to an ICCD	14
3.2 New Difficulties	17
IV. Experimental Methods and Analysis	23
4.1 Camera Parameters	23
4.2 Camera Data Analysis	33
4.3 Crosstalk Analysis	39
V. Final Results and Conclusion	43
5.1 Final Results	43
5.2 Conclusion	45
BIBLIOGRAPHY	48

LIST OF TABLES

Table

4.1	Binning Noise Analysis 3ms DT	31
4.2	Asymmetric Binning Noise Analysis 3ms DT	32

LIST OF FIGURES

Figure

2.1	Ytterbium 171+ Energy Levels	5
2.2	Ideal Ion Detection Distributions	5
2.3	Off-Resonant Coupling Photon Distributions	8
2.4	Exponential Fit to Bright Ion Going Dark	10
2.5	Photon Distributions of Many Ions and Overlap	13
3.1	Intensifier Quantum Efficiency Curve	15
3.2	Diagrams of Multi-Channel Plate	16
3.3	Diagram of an ICCD	18
3.4	Gaussian Fit to Ion Spot on CCD	21
4.1	Photon Distributions for Bright and Dark Ions with/out Background Scatter . . .	24
4.2	Photon Distributions for Multiple Detection Times with Background	25
4.3	Theoretical State Detection Error vs. Detection Time	26
4.4	State Detection Error with Camera versus Detection Time	26
4.5	Interline CCD Readout Diagram	28
4.6	2x2 Binning Diagram	29
4.7	State Detection Error with Camera versus Hardware Binning	32
4.8	State Detection Error with Camera versus Asymmetric Hardware Binning	33
4.9	Signal Contribution of Ions to Other Positions	35
4.10	Summed Single Row Data and 1-D Gaussian Fit	37
4.11	Average Value of Correlation Function along Ion Chain	40
4.12	Correlation Function Values for Different Positions on Ion Chain	42

5.1	PMT Histogram of Dark and Bright Ion	44
5.2	Many Ion Rabi Flopping	46

ABSTRACT

YTTERBIUM ION QUBIT STATE DETECTION ON AN ICCD CAMERA

by
Aaron C. Lee

Chair: Christopher R. Monroe

Feynman's proposal in 1982 that a well-controlled quantum system could efficiently simulate another quantum system [1], confirmed by Lloyd in 1996 [2], has been realized in many different physical implementations. The requirement of a stable, coherent platform with controllable interactions has been shown to be fulfilled by many different types of systems, one of which is a trapped atomic ion. We use $^{171}\text{Yb}^+$ where the qubit states are the hyperfine ground states, $^2S_{1/2} |F = 1, m_F = 0\rangle$ and $|F = 0, m_F = 0\rangle$. DiVincenzo's requirements for a quantum information system also include accurate read out of the the qubits [3]. In the case of our system, this means measuring the scattered photons of the stimulated $^2S_{1/2} |F = 1, m_F = 0\rangle$ to $^2P_{1/2} |F = 0, m_F = 0\rangle$ transition. Previously, we have used a photo-multiplier tube for the detection of these photons. In this work, I present the analysis of a new detection device, a PIMax3: 1024i ICCD camera, and the state detection fidelity of our qubits with this camera. With the optimal settings of a 3ms detection time and a hardware binning of 4x64, our state detection fidelity was found to be approximately 95%. While the fidelity is slightly worse than the PMT at 97%, the ability to measure spin order and perform shot to shot discrimination are a notable improvement to the quantum simulator.

CHAPTER I

Introduction

In 1982, Richard Feynman proposed that a well-controlled quantum system could efficiently simulate another quantum system which could not be described classically [1]. This was later confirmed by Seth Lloyd in 1996 [2]. Thus, a quantum simulator is capable of simulating a many-body quantum system that is impossible to understand analytically and improbable to simulate numerically due to the prohibitive computational resources required.

One possible kind of quantum simulator can be thought of as the quantum version of an analog computer. An analog computer uses physical phenomena, such as electricity, to model a given problem. Thus an analog computer might use a varying resistance to simulate a changing stiffness in a spring. This is different from a digital computer where the system being modeled is converted into binary numbers and its evolution is simply a series of digital logic operators performed on the initial numbers. In the analog computer, there are no 1's and 0's, only changing physical quantities.

Much like the analog computer, an analog quantum simulator would model a more complex system by constructing an equivalent situation on a simpler setup. This is distinct from the quantum computer, which would represent the system in a qubit register and apply quantum operations (quantum gates) stroboscopically to produce

the result. Using an analog quantum computer, we can simulate poorly understood models from condensed matter, such as quantum magnetism [4], spin glasses [5], spin liquids [6], and high temperature superconductors [7, 8]. In particular, quantum spin models are able to describe a large set of quantum many-body problems. Some of these many-body problems fall into the class of NP-Complete, which is a class of problems where the time required to solve the problem is extremely long with classical algorithms [9, 10].

One approach toward the realization of such a quantum simulator is to apply ideas from adiabatic quantum computation, where a known, trivial Hamiltonian is adiabatically transformed to the ground state of the desired Hamiltonian [11, 12]. In order to achieve such an adiabatic transformation, a quantum simulator requires a stable, coherent platform which has controllable interactions. Some systems that have been shown to have these properties are superconducting circuits [13, 14, 15], quantum dots [16], neutral atoms [17, 18, 19, 20, 21], and trapped atomic ions [22, 23, 24, 25, 26, 27, 28, 29, 30, 31].

In 2000, DiVincenzo [3] laid out what was required for a quantum computer. Many of the same requirements apply to a quantum simulator. One of these requirements was the accurate read out of the qubits. In this paper, we will focus on the qubit readout by analyzing the characteristics and state detection of a Princeton Instruments PIMax: 1024i ICCD camera and comparing it to the current detection method, which is a PMT.

CHAPTER II

Ytterbium Detection

2.1 The Detection Transition

Any two-level quantum system can be mapped to a spin-1/2 model in an effective magnetic field [32, 33, 34]. Our system represents a spin-1/2 system by the two hyperfine ground states of $^{171}\text{Yb}^+$, $^2S_{1/2} |F = 1, m_F = 0\rangle$ and $|F = 0, m_F = 0\rangle$, which are separated by $\nu_{HF}/2\pi = 12.643$ GHz [35]. F is the quantum number representing the atomic angular momentum and m_F is its projection along a weak magnetic field of approximately 4 Gauss. We define the $|F = 1, m_F = 0\rangle$ to be $|\uparrow_z\rangle$ and the $|F = 0, m_F = 0\rangle$ to be $|\downarrow_z\rangle$ of σ_z . Detection of the ion state uses a standard spin-dependent resonant fluorescence cycling on the $^2S_{1/2}$ to $^2P_{1/2}$ transition at 369.53 nm, which is shown in Figure 2.1. The detection light is resonant with ions in $|\uparrow_z\rangle$ and will scatter many photons whereas the detection light is far off-resonant with ions in $|\downarrow_z\rangle$. Further, the energy difference between $|F = 1, m_F = \pm 1\rangle$ and $|F = 1, m_F = 0\rangle$ of the $S_{1/2}$ manifold is $\delta_{zeeman} = (1.4 \text{ MHz/Gauss}) B_z$ where B_z is the magnetic field in Gauss. Since the magnetic field at the ion chain is approximately 4.8 Gauss, δ_{zeeman} is only about 6.7 MHz for the $^2S_{1/2} |F = 1, m_F = \pm 1\rangle$ in our system and natural linewidth of the $^2P_{1/2} |F = 0, m_F = 0\rangle$ transition is $\gamma/2\pi = 20$ MHz, the $m_F = \pm 1$ states are also resonantly excited to the $P_{1/2}$ manifold. Thus a bright ion

will scatter many photons in a single detection cycle while the probability of $|\downarrow_z\rangle$ being off-resonantly excited is very low. In addition to the off-resonant transition to the dark state, there is a 0.5% chance that the $^2P_{1/2}$ state can decay to $^2D_{3/2}$. This state has a lifetime of approximately 52.7 ms, which is long compared to the detection time of the ions. Therefore, we apply 935.2 nm light to the ion, which pumps it from $^2D_{3/2}$ to $^3[3/2]_{1/2}$, which has a life-time of 37.7 ns and a 98.2% chance to decay back to the $^2S_{1/2}$ F=1 manifold. Due to the fact that we pump to the F=0 line of the bracket state, selection rules prevent the electron from decaying down into the $|\downarrow_z\rangle$. This way, we are able to pump out of the D manifold without mixing the bright state with the dark state. Finally, there is a F-state which has a lifetime much longer than a minute and which can become populated. This transition is actually an octopole transition and is typically forbidden, but if the ion is hit by a background gas molecule while the electron is in the excited state, the electron can populate this state. In order to recover the ion to the bright and dark states, we apply a laser with a wavelength of 638.6 nm. This pumps the ion back to the $^2D_{3/2}$, where the 935 nm beam pumps it back down to the $^2S_{1/2}$ state.

2.2 Off-Resonant Coupling

In the ideal case, the number of detected photons from the ions will follow Poissonian statistics. Based on the detection time, the scattering rate of the $^2P_{1/2}$ will determine a mean number of photons emitted, λ_0 . Thus, the collected photon distributions would have the form:

$$p_{bright,ideal}(n) = \frac{e^{-\lambda_0} \lambda_0^n}{n!} \quad (2.1)$$

This equation gives the probability of detecting n photons during a detection cycle. An example of what would be seen on the PMT is shown in Figure 2.2.

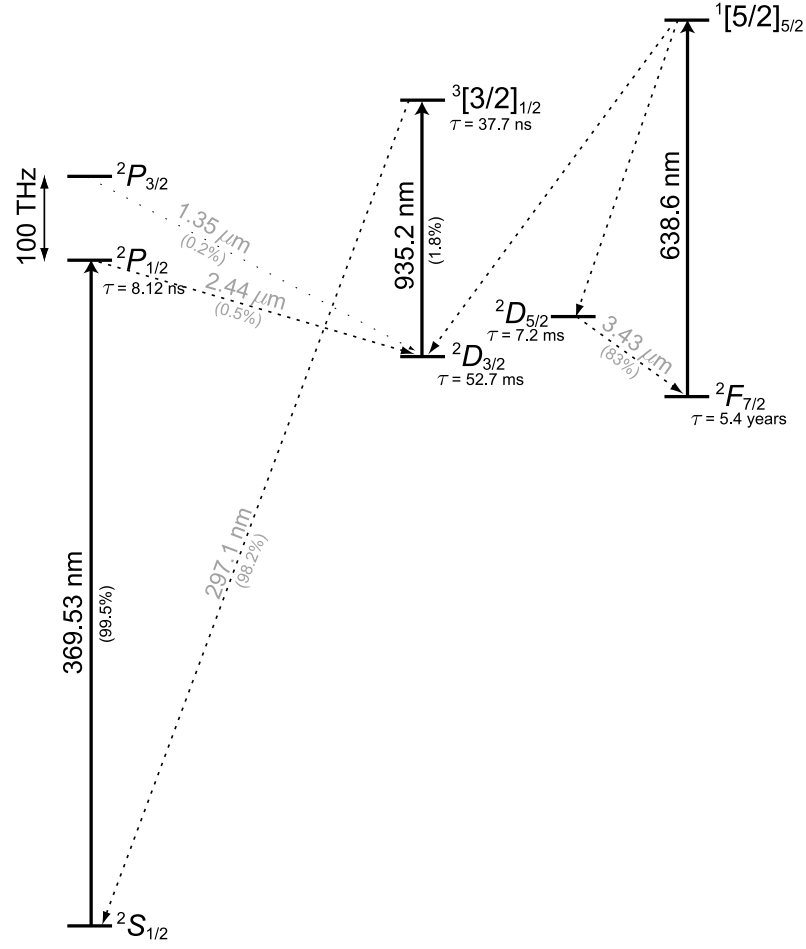


Figure 2.1: Ytterbium 171+ Energy Levels. This diagram shows the different energy levels that are relevant to the detection transition

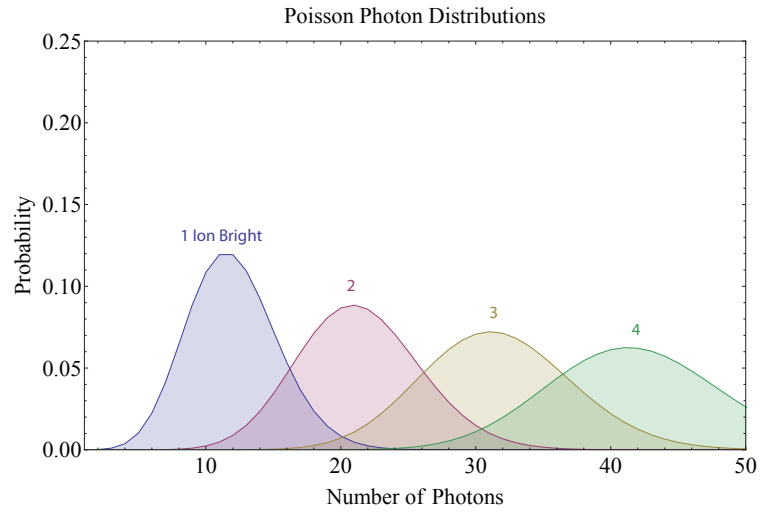


Figure 2.2: Ideal Ion Detection Distributions. This figure shows the photon distributions of an ideal detection transition where there is no off-resonant coupling for different ion numbers

While the decay to the D-manifold does not lead the bright state to couple with the dark state, off-resonant coupling of the two states still occurs, requiring that the ideal distributions of the bright ion be modified. The rate equations which describe this coupling yield an exponential probability distribution. Thus the ion, which is initially in the bright state but off-resonantly couples to the dark state, will have a distribution of emitted photons that is a convolution of a Poissonian and exponential distributions [36, 37, 38]. The probability that an ion in the bright state will leave the bright state in a time interval $t + dt$ is given by:

$$f(t)dt = \frac{1}{\tau_{L_2}} e^{-\frac{t}{\tau_{L_2}}} dt \quad (2.2)$$

τ_{L_2} is the average leak time of the bright state into the dark state. τ_{L_2} is determined by the properties of the ion and the intensity of the detection light. Further, the average number of collected photons for a bright ion that is pumped dark at a time t is:

$$\lambda(t) = \frac{t}{\tau_D} \lambda_0 \quad (2.3)$$

where τ_D is the detection time and λ_0 is the mean number of photons collected for that detection time. Using equation 2.3, we are able to get t as a function of λ . This can then be substituted into equation 2.2. The result is the probability of the bright state producing a Poissonian distribution of collected photons with mean λ :

$$g(\lambda)d\lambda = \begin{cases} \frac{\alpha_2}{\eta} e^{-\lambda\alpha_2/\eta} d\lambda & \lambda < \lambda_0 \\ e^{-\alpha_2\lambda_0/\eta} & \lambda = \lambda_0 \end{cases} \quad (2.4)$$

where $\eta = \eta_D \frac{d\Omega}{4\pi} T$ is the total photon collection efficiency determined by the detector efficiency (η_D), the solid angle of collection ($\frac{d\Omega}{4\pi}$), and the optical transmission from the ion to the detector (T); $\alpha_2 \equiv \frac{\tau_D \eta}{\tau_{L_2} \lambda_0}$ is the coupling probability per emitted photon; and the $\lambda = \lambda_0$ discontinuity is required to account for the portion of ions that do

not leave the bright state. Therefore, the probability of detecting n photons will be the convolution of the probability of producing the distribution with the Poisson distribution:

$$p_{bright}(n) = \left(\frac{e^{-\lambda_0} \lambda_0^n}{n!} \right) e^{-\alpha_2 \lambda_0 / \eta} + \int_0^{\lambda'} \frac{e^{-\lambda} \lambda^n}{n!} \frac{\alpha_2}{\eta} e^{-\lambda \alpha_2 / \eta} d\lambda \quad (2.5)$$

where $\lambda' = \lambda_0 - \epsilon$ and $\epsilon \ll 1$. In the limit where $\lambda' \Rightarrow \lambda_0$, the probability distribution converges to the lower incomplete gamma function, $\Gamma_{lower}(a, x) \equiv \frac{1}{(a-1)!} \int_0^x e^{-y} y^a dy$ which is the standard definition of the incomplete Gamma function normalized such that $\Gamma_{lower}(a, \infty) = 1$. Let $\lambda^* = (1 + \alpha_2/\eta)\lambda$ in the limit where $\lambda' \Rightarrow \lambda_0$, the equation becomes:

$$p_{bright}(n) = \left(\frac{e^{-\lambda_0} \lambda_0^n}{n!} \right) e^{-\alpha_2 \lambda_0 / \eta} + \alpha_2 / \eta \int_0^{(1+\alpha_2/\eta)\lambda_0} \frac{e^{-\lambda^*} (\lambda^*)^n}{(1 + \alpha_2/\eta)^n n!} \frac{d\lambda^*}{(1 + \alpha_2/\eta)}$$

Rewriting equation 2.5 in terms of Γ_{lower} , where $a = n + 1$ and $y = (1 + \alpha_1/\eta) \lambda_0$,

$$p_{bright}(n) = \frac{e^{-(1+\alpha_2/\eta)\lambda_0} \lambda_0^n}{n!} + \frac{\alpha_2/\eta}{(1 + \alpha_2/\eta)^{n+1}} \Gamma_{lower}(n + 1, (1 + \alpha_1/\eta) \lambda_0) \quad (2.6)$$

In a similar way, a dark ion can off-resonantly couple to the bright state. Just as for the bright state, the photon probability distribution is a convolution of the exponential probability of the dark state going bright and the Poissonian distribution. Yet for the dark state, the emission is flipped: the ion will not scatter photons on the closed transition, but at some time, the ion will be pumped into the bright state and begin to emit photons. Let probability of leaking to the bright state per emitted photon be defined as $\alpha_1 \equiv \frac{\tau_D \eta}{\tau_{L1} \lambda_0}$ where τ_{L1} is the average coupling time of the dark state. By a similar analysis as before, the probability of detecting n photons from a dark ion is:

$$p_{dark}(n) = e^{-\alpha_1 \lambda_0 / \eta} \left[\delta_n + \frac{\alpha_1 / \eta}{(1 - \alpha_1 / \eta)^{n+1}} \Gamma_{lower}(n + 1, (1 - \alpha_1 / \eta) \lambda_0) \right] \quad (2.7)$$

A plot of both p_{dark} and p_{bright} can be seen in Figure 2.3.

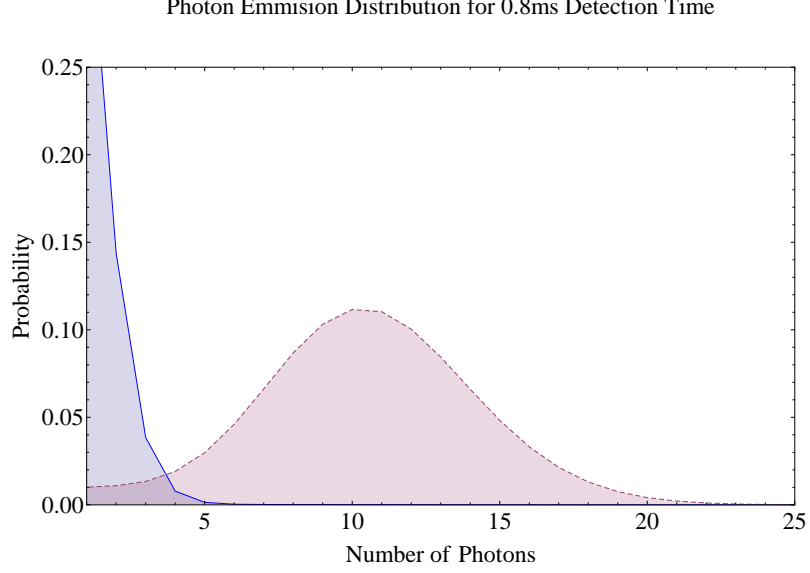


Figure 2.3: Off-Resonant Coupling Photon Distributions. This figure shows the photon distributions of the bright and dark ions with the addition of the off-resonant coupling.

2.3 Finding α_1 and α_2

Since the laser power is split equally across all three polarizations to prevent the population of a dark eigenstate, the mean number of collected scattered photons for a bright ion is:

$$\lambda_0 = \tau_D \eta \frac{s \frac{\gamma}{2}}{1 + s + \left(\frac{2\delta}{\gamma}\right)^2} \quad (2.8)$$

where γ is the radiative linewidth of the $P_{1/2}$ state, δ is the detuning of the light from the transition and $s = \frac{I}{I_{sat}}$ is the laser-ion saturation parameter.

The definition for α_1 is:

$$\alpha_1 \equiv \frac{\tau_D \eta}{\tau_{L_1} \lambda_0} \quad (2.9)$$

Yet $\frac{1}{\tau_{L_1}}$ can be re-expressed as:

$$\frac{1}{\tau_{L_1}} = \gamma_{L_1} = \mathbf{M}_1 \frac{s \frac{\gamma}{2}}{1 + s + \left(\frac{2\Delta_1}{\gamma}\right)^2} \quad (2.10)$$

where \mathbf{M}_1 is the branching ratio for the off-resonant coupling and Δ_1 is the detuning

of the resonant transition from the off-resonant transition. Since $\Delta_1 \gg \gamma$,

$$\gamma_{L_1} \approx \mathbf{M}_1 s \frac{\gamma}{2} \left(\frac{\gamma}{2\Delta_1} \right)^2 \quad (2.11)$$

Therefore, substituting equation 2.8 and 2.11 into equation 2.9, we get:

$$\alpha_1 = \mathbf{M}_1 \left[1 + s + \left(\frac{2\delta}{\gamma} \right)^2 \right] \left(\frac{\gamma}{2\Delta_1} \right)^2 \quad (2.12)$$

In the case of the $^{171}\text{Yb}^+$ ion, the radiative linewidth of the $S \rightarrow P$ transition is $\gamma/2\pi = 20$ MHz and the detuning of the dark state from the excited state which couples to the bright state is $\Delta_1 = \omega_{SHF} + \omega_{PHF}$ where ω_{SHF} is the hyperfine splitting in the $^2S_{1/2}$ state and ω_{PHF} is the hyperfine splitting of the $^2P_{1/2}$ state. These values are $\omega_{SHF}/2\pi = 12.643$ GHz and $\omega_{PHF}/2\pi = 2.105$ GHz for a total $\Delta_1/2\pi = 14.748$ GHz. Further, all allowed dipole transitions have the same relative strength and selection rules only allow $^2P_{1/2} |F=1\rangle$ to couple with $^2S_{1/2} |F=1\rangle$ in only 2 ways no matter the polarization, the dark state leakage branching ratio is: $\mathbf{M}_1 = 1/3 \times (1/3 + 1/3) = 2/9$. Substituting to α_1 and assuming that $s \approx 1$ and $\delta \ll \gamma$,

$$\begin{aligned} \alpha_1 &\approx 4/9 \left(\frac{20}{2 \times 14.748 \times 10^3} \right)^2 \\ &= 2.04 \times 10^{-7} \end{aligned}$$

Using a similar calculation, we can find α_2 :

$$\alpha_2 = \mathbf{M}_2 \left[1 + s + \left(\frac{2\delta}{\gamma} \right)^2 \right] \left(\frac{\gamma}{2\Delta_2} \right)^2 \quad (2.13)$$

where $\Delta_2 = \omega_{PHF}$ and $\mathbf{M}_2 = 2/9$ for the same reason as \mathbf{M}_1 . α_2 is then calculated to be: $\alpha_2 = 1.00 \times 10^{-5}$. The reason that α_1 and α_2 are different is that the detunings are different when the bright ion is going dark and the dark ion is going bright.

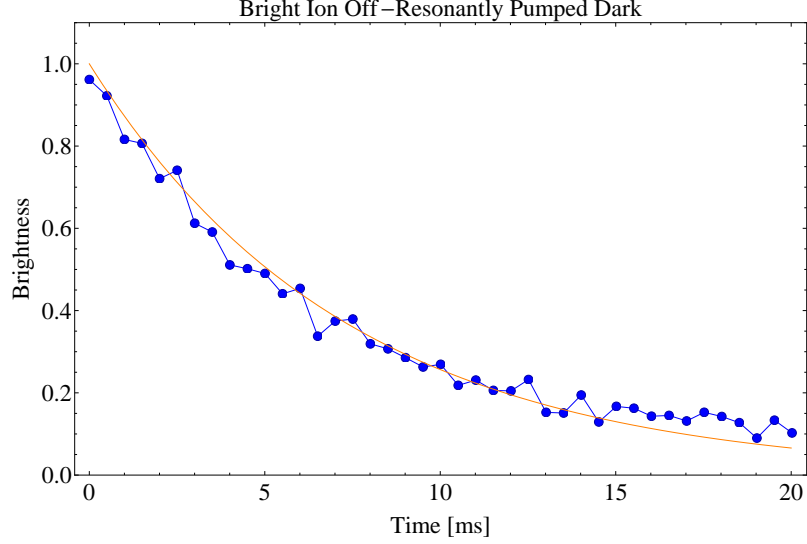


Figure 2.4: Exponential Fit to Bright Ion Going Dark. In this figure, the blue points represent the data points and the red plot represent the exponential fit. The resultant average decay is $\tau_{L_2} = 7.35\text{ms}$

These values for α_1 and α_2 are in the limit where $s=1$. The intensity of the detection beam at the ion is not exactly the same as I_{sat} , so the true values for α_1 and α_2 are difficult to calculate unless s is well known. Another approach is to experimentally measure α_1 and α_2 . For α_2 , this measurement is simple. We first initialize the ion into the bright state and then expose the ion to the resonant detection light for longer and longer periods of time. Finally, we detect to see whether the ion is still bright or not. If we then plot the probability of the ion being bright vs exposure time, there will be an exponential decay. Thus, τ_{L_2} will be the width of this decay. Using this method, we found $\tau_{L_2} = 7.35$ ms. The data and fit can be seen in Figure 2.4. The exponential fit does not work in the case of τ_{L_1} since τ_{L_1} is much longer than τ_{L_2} , meaning that we see second order effects of a dark ion going bright and then going dark again. If we calculate the τ_{L_2} directly:

$$\frac{1}{\tau_{L_2}} = \gamma_{L_2} \approx \mathbf{M}_2 s \frac{\gamma}{2} \left(\frac{\gamma}{2\Delta_2} \right)^2 \quad (2.14)$$

where we are again assuming that $\Delta_2 \gg \gamma$. If s is assumed $s=1$, then we get

$\tau_{L_2} = 3.32$ ms. Using these values, since $\gamma_{L_2} \propto s \rightarrow \tau_{L_2} \propto \frac{1}{s}$, we can calculate what the intensity is at the ion, which turns out to be $I = 45\% I_{sat}$.

We can now find the actual values of α_1 and α_2 , still under the assumption that $\delta \ll \gamma$, namely that:

$$\alpha_1 = 1.48 \times 10^{-7} \quad (2.15)$$

$$\alpha_2 = 7.27 \times 10^{-6} \quad (2.16)$$

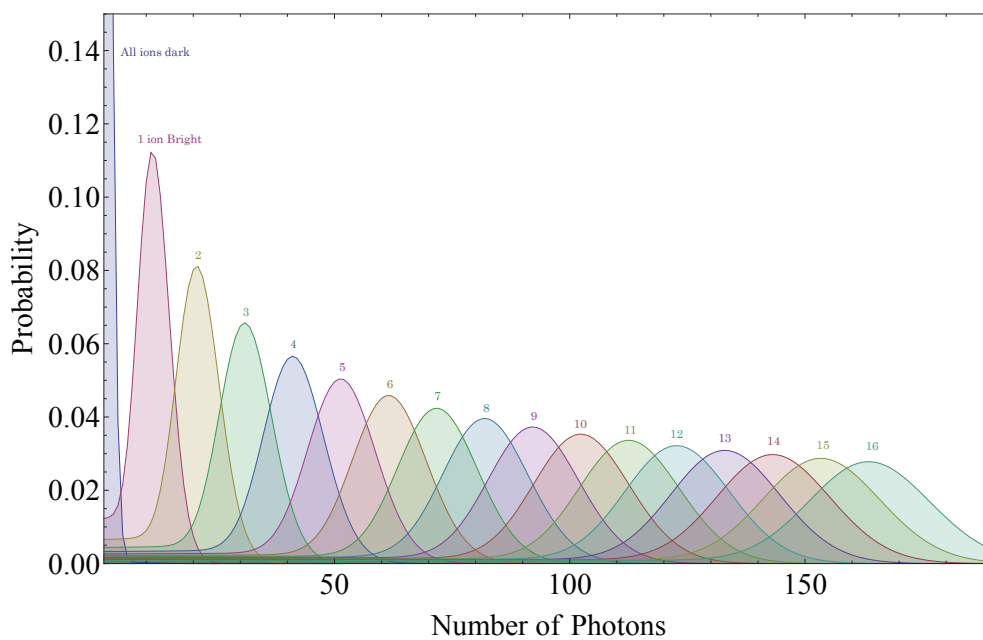
2.4 Detection with the PMT

In the past, the primary device used for detection on our experiment has been a photo-multiplier tube (PMT). A PMT is a very efficient way to detect low numbers of photons, as it converts single photons into an electron cascade. The cascade is then converted into a voltage, typically using operational amplifiers. This voltage then produces a TTL pulse, which is counted. Since the PMT does not have to read out a large number of pixels, the speed of the conversion of the photon into a signal is extremely fast. By taking a hundred or more experiments, a distribution of the photons can be accumulated and compared to the theoretical distributions described above. Due to its speed and efficiency, the PMT has been the optimal method of detecting the state a small number of ions. Yet, two major limitations of the PMT have motivated the introduction of a new detection apparatus.

The first limitation is that the PMT has no spatial discrimination. The signal from the PMT is the same if ion number 1 is bright and the rest are dark or if ion number n is bright and the rest are dark. This inhibits our ability to study dynamics in the ion chain. Most dynamics consist of watching excitations propagate in our system or watching domains change in the ion chain or measuring the spin-order. Without spatial discrimination, we are unable to observe these effects.

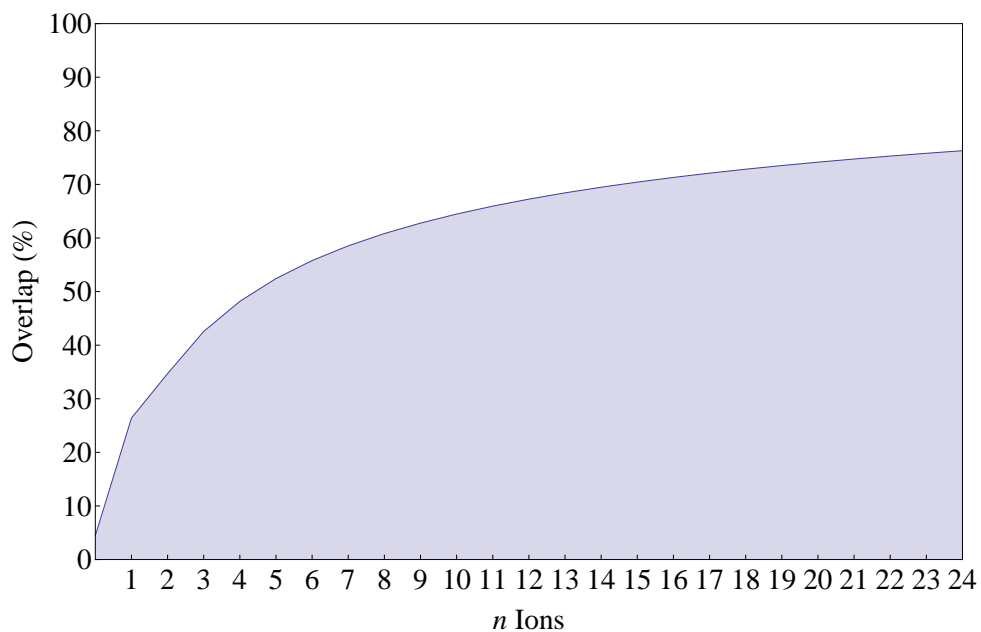
The second limitation is that the PMT can only measure the average number of bright ions. Further, the PMT can only measure the average number of ions well for up to 8 or 9 ions in the trap. For a greater number of ions, the overlap of the “ n ions” bright state and the “ $n + 1$ ions” bright state becomes extremely high. This is illustrated in Figure 2.5. For 15 and 16 ions, the overlap is over 60%, meaning that we are unable to know for certain whether 15 or 16 ions are bright. Knowing only the average number of bright ions further limits us by the increase in the degeneracy of states as the number of bright ions approaches half. If only half the ions are bright, there are $\binom{N}{N/2}$ possible arrangements of the bright ions. We are thus prohibited from studying models where the spin ordering is required, since we would be unable to distinguish, for example, $|\uparrow\downarrow\uparrow\downarrow\rangle$ from $|\downarrow\uparrow\uparrow\downarrow\rangle$, $|\uparrow\downarrow\downarrow\uparrow\rangle$, etc. Considering the physics which can be studied without these limitations, a new detection apparatus is required.

Photon Emission Distribution Depending on Number of Ions



(a) Many Ion Photon Distributions

Overlap of Photon Distribution between n Ions and $n+1$ Ions



(b) Overlap of n Ions and $n + 1$ Ions

Figure 2.5: Photon Distributions of Many Ions and Overlap. In Figure 2.5a, many ion photon distributions are shown. Below, the overlap of the n th ion and the $(n + 1)$ th ion are shown.

CHAPTER III

The ICCD Camera

3.1 Introduction to an ICCD

An Intensified Charge-Coupled Device (ICCD) was originally developed by the military for night vision technology. While this application is very different from the ICCD's original purpose, the components are relatively similar. They are broken into four distinct parts: the photocathode, the multi-channel plate (MCP), the phosphor screen, and finally the charge-coupled device (CCD).

The photocathode is the part of the device which specializes the ICCD to a particular use, e.g. night vision or ion state detection. The photocathode takes an incident photon and converts it into an electron. This process has a quantum efficiency which describes the probability of this interaction. The quantum efficiency is extremely dependent on the wavelength of the incident photons. In our case, the photocathode was coated so that it would respond well to 369nm wavelength light, which corresponds to the detection transition of the bright ions. A plot of the quantum efficiency relative to wavelength can be seen in Figure 3.1.

This single photo-electron from the photocathode is then run through a multi-channel plate (MCP). This plate acts like a photomultiplier and exponentially increases the number of the electrons. The MCP is made out of a porous glass substrate

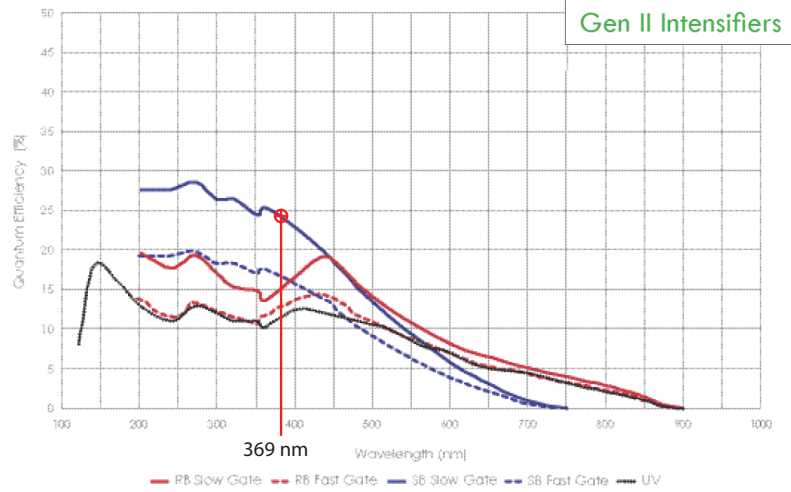
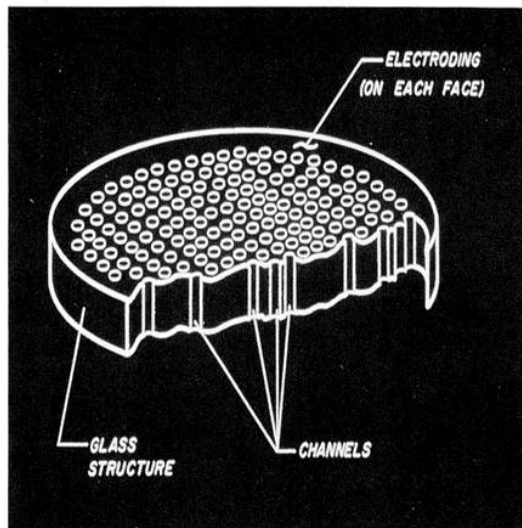


Figure 3.1: Intensifier Quantum Efficiency Curve. Courtesy of Princeton Instruments

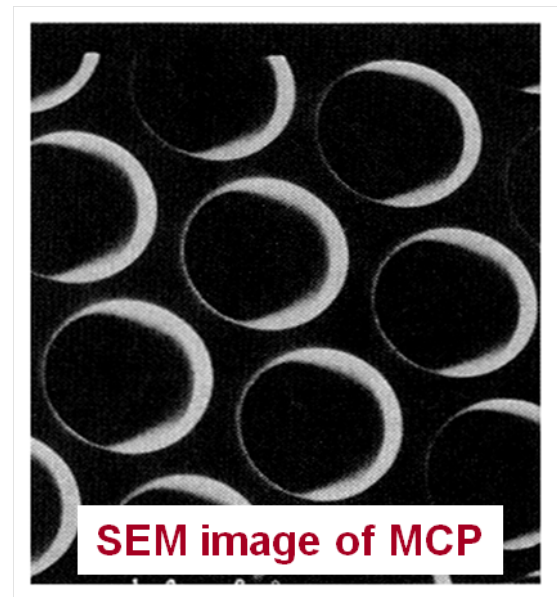
with a secondary electron emitter which coats the inner surface of the pores. The pores of this glass substrate are actually angled so that a photo-electron that enters one of the pores normal to the surface will collide with the side of the pore, generating the electron cascade. These pores typically have a diameter ranging from $6\mu\text{m}$ - $12\mu\text{m}$. Diagrams of an MCP can be seen in Figure 3.2. This system does reduce overall quantum efficiency due to the fact that the MCP has a finite density of pores, and thus some photo-electrons are lost since they strike the glass substrate between the pores. By increasing the size of the pores, the electron loss is reduced at the cost of resolution.

The photoelectron cascade then falls on a phosphor screen. The phosphor is excited by the electron cascade and so emits light. The emitted light emits in a spectrum which has a sharp peak around the optimal wavelength for the CCD. Thus the electron cascade is converted into a photon cascade. The single detected photon has now been exponentially increased into a shower of green photons. These three components are often referred to as the intensifier.

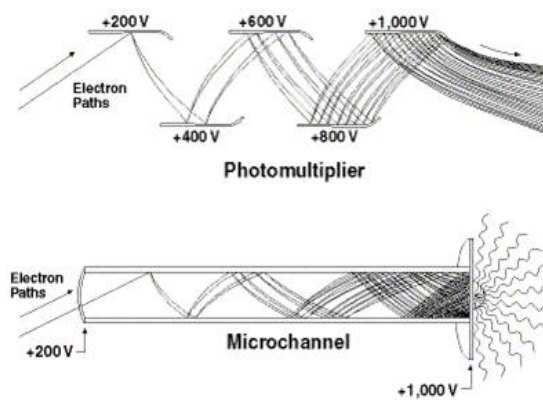
The light coming off of the phosphor screen must be focused onto the CCD in



(a) MCP Schematic



(b) Zoomed In MCP



(c) MCP vs PMT Diagram

Figure 3.2: Diagrams of Multi-Channel Plate. Courtesy of Princeton Instruments.

order to prevent the image from being distorted or blurred. This can be accomplished by either of two methods: lens coupling or fiber coupling. Lens coupling involves using a lens to image the phosphor screen onto the CCD. The primary advantage of lens coupling is that the intensifier can be removed. The drawback is that there is lower light throughput (5%-10%) and greater stray light detection. A fiber coupled intensifier uses optical fibers to focus the light down onto the CCD. This method has a greater throughput (60%) but requires a dry, non-vacuum operating environment to operate and is permanently bonded to the CCD.

The heart of the camera is the Charge-Coupled Device (CCD), which takes the phosphor photon cascade and turns the photons back into photo-electrons. The CCD works much like a photodiode but is broken up into many pixels. These pixels accumulate charge in the presence of light. This charge is then pushed around by changing voltages in the pixels. In this way, the CCD can shift the charge from the pixel to an Analog to Digital device, which converts the charge to a numerical value, all the while maintaining the separate individual pixels. Our camera is a PIMax3:1024i made by Princeton instruments. It has a Kodak KAI-1003 scientific grade interline CCD. This CCD has 1024 x 1024 imaging pixels, where each pixel is 12.8 x 12.8 μm in size. The whole CCD is 13.1 x 13.1 mm. The intensifier is a Gen II Super Blue. The overall quantum efficiency of the camera is specified as $\approx 20\%$ for 360 nm.

3.2 New Difficulties

While the PIMax3:1024i ICCD camera will solve some of the issues that the PMT has with single shot discrimination and large ion chains, the camera also introduces new problems into the state detection. These difficulties can be categorized as de-

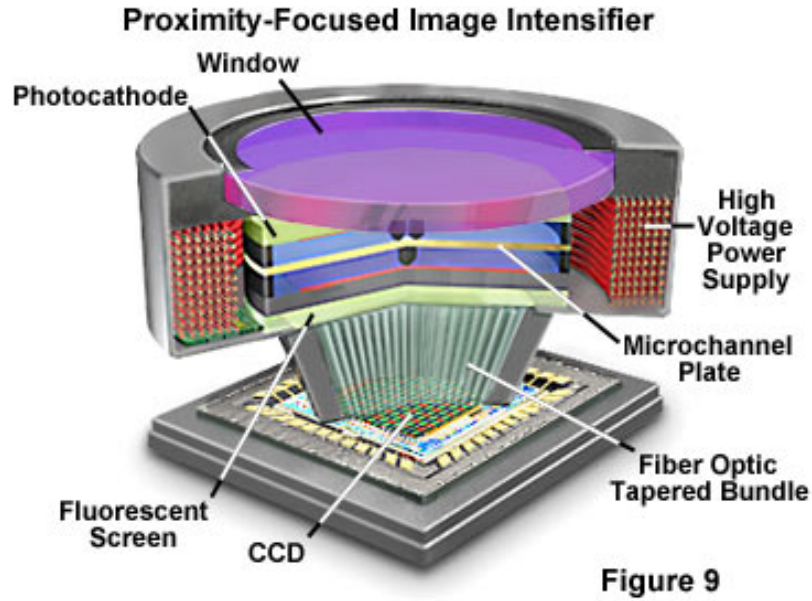


Figure 3.3: Diagram of an ICCD. Courtesy of Olympus America Inc.

tection time and error.

The issue of time enters only as a practical matter. Large numbers of data points are required to recover the probability distribution of the quantum system. Thus, as the amount of time needed for each experiment increases, the likelihood that a background gas molecule will collide with the ion chain, causing them to decrystallize and possibly evaporate from the trap, grows. The difficulty increases with more ions in the trap, so keeping the time for each experiment minimal is extremely important as we increase the ion number. The matter of experimental duration is not an issue when using the PMT for detection as its readout time is effectively the exposure time.

The camera also introduces new sources of error, as it is much more complex than the PMT. There are more losses in the camera, since a photon event at the intensifier does not necessarily lead to a signal of definite size at the CCD (e.g. the photo-electron might not create a cascade on the MCP). While not ideal, this type of issue can just be factored into the overall quantum efficiency of the camera: namely

the signal is slightly smaller than an ideal system. The error which is more serious comes from two sources: analog to digital conversion error and crosstalk.

Analog to digital conversion (ADC) error is the fluctuation in the digital numerical value of the accumulated charge on the CCD. When the CCD is “read out”, each pixel of accumulated charge is fed into a device which compares the voltage on the pixel to a reference voltage and then produces a binary number to represent the charge on the pixel. This operation has a fundamental limit in that the resolution of the device is much larger than the magnitude of the charge of a single electron, and additionally the ADC also is affected by fluctuations in the reference voltage or by uncertainty in the comparison to the reference voltage. There are also variations in the readout due to shot noise, dark current, and Johnson noise. Ultimately, each pixel is going to have some fluctuation in its value due to these sources. In the limit of small signals that we are working with, these fluctuations can be as large as the signal itself. The PMT is also affected by similar noise sources, but has the benefit that the signal is continuously read out and, since its readout is a simple TTL pulse, it is not sensitive to fluctuations in the photo-electron cascade. Thus the PMT eliminates one of the largest sources of error in the camera, but at the sacrifice of spatial resolution.

While spatial resolution is one of the primary reasons for the use of the camera over the PMT, it also introduces a new source of error into the state detection of the ion, namely ion crosstalk. Ion crosstalk is the light from one ion creating a signal at a neighboring ion’s location. As the number of ions in the trap increases, the space between the ions decreases, which is problematic. The shrinking distance between ions increases the amount of crosstalk between neighboring ions to the point where a dark ion can be evaluated as bright because of the cross talk from its bright

neighbors. This crosstalk comes about from two sources: the imaging optics and the finite resolution of the camera.

In order to image the ions in the trap, we use an objective with a numerical aperture $NA = 0.24$. Thus a perfect point imaged by our objective with a 1-1 magnification will now have an Airy disk with a width of x where x is:

$$\begin{aligned} x &= 1.22 * \frac{1}{2NA} * \lambda \\ &= 1.22 * 2.1 * 369nm \\ &= 0.95\mu m \end{aligned}$$

Thus you can see that what was a perfect point now has a diameter of $2x = 1.9\mu m$. But since the separation of the ions is around $2-5\mu m$ depending on the number of ions in the trap and the magnitude of the endcap voltages and the pixel size of the CCD is $12.8 \times 12.8\mu m$ in size, the image of the ion chain is magnified approximately 130x, giving a separation of the ions at around $160-650\mu m$ with an ion diameter of $247\mu m$. These values assume that the optics of the imaging system have no aberrations. In order to find out what the size of the ion is with actual optics, a thousand images of a single ion were averaged and summed down to a 1 dimensional row. This averaged data was then fit with a Gaussian distribution of $e^{\frac{-2(x-x_0)^2}{w^2}}$ where w is the waist, namely the radius at which the intensity is $1/e^2$ of its peak value. We found w to be approximately $250\mu m$. The fit can be seen in Figure 3.4. Clearly then we are diffraction limited by the objective and not aberration limited by our optics. Yet the separation of the ions shrinks with the number of ions. As the system size increases, the ions begin to overlap and the signal from one ion begins to fall onto the region of the CCD occupied by its neighbor. A profile of $250\mu m$ is going to have a significant overlap with the nearest neighbor when separated only by $160\mu m$ on the CCD. While

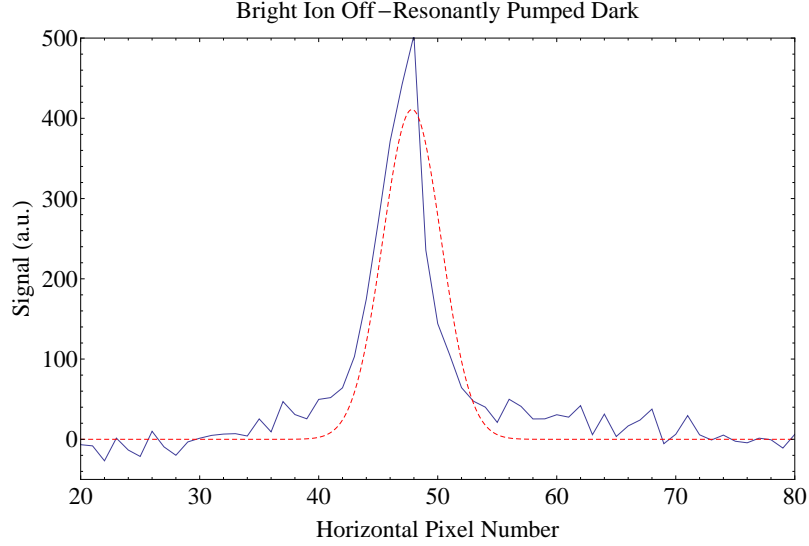


Figure 3.4: Gaussian Fit to Ion Spot on CCD. Here are shown a summed down 1 dimensional row data in blue and the approximation using a Gaussian fit $e^{\frac{-2(x-x_0)^2}{w^2}}$ to find the waist in red. Thus the waist, w is at e^{-2} . The waist found was $w = 250\mu m$.

these aberrations will always be present in any optics, they might be diminished by a larger numerical aperture of the objective, but larger numerical aperture objectives are prohibitively expensive. The size of the ion on the CCD is further increased by the finite resolution of the camera. This means that whatever the size of the ion is from the imaging optics, the size on the CCD is increased due to the size of the pixels since any signal that falls on a given pixel will then have the size of that pixel, regardless of where the photon strikes. This will have its greatest effect at the outer edges of the Airy disk, spreading out the edges of the disk. Clearly though, we are in a regime where the finite numerical aperture is limiting our imaging, not the resolution of the camera.

For the purposes of our experiment, the state detection error of the ion must be minimized as much as possible. This error is especially important when working with larger numbers of ions because $\epsilon_N = \epsilon^N$, where the detection fidelity of the spin order of N spins is ϵ_N and ϵ is the single ion detection fidelity. Thus, if our detection

fidelity was $\epsilon = 94\%$ for a 10 ion spin order, the detection fidelity for the entire chain would be $94\%^{10} = 54\%$, whereas if the detection fidelity is increased by only 2%, the entire chain spin order detection fidelity becomes $96\%^{10} = 66\%$. Clearly an increase of 10% is quite significant and so the optimization of our detection fidelity on the camera becomes extremely important as the system size increases.

CHAPTER IV

Experimental Methods and Analysis

4.1 Camera Parameters

4.1.1 Detection Time The detection time of the camera is simply the length of time which the camera is exposed to the fluorescence of the resonantly excited ion. Changing the detection time implies that the length of time which the ion is exposed to the resonant light changes and the length of time which the intensifier is active changes. The length of time over which the intensifier is active simply determines how long the camera integrates and so longer times mean more collected photons. On the other hand, changing the length of time over which the ion is exposed has further ramifications, per the discussion in Chapter II, since increasing the detection time increases the probability of the bright ion going dark. Increasing the detection time also increases the amount of background scatter collected. The background scatter shifts the dark state out from the 0 bin, which begins to overlap more and more with the bright state, leading to a reduction in state discrimination. The background scatter also changes the shape of the bright state.

In order to find how the background scatter affects the measured photon distribution, we first start with the bright state and dark state distributions in equations 2.7 and 2.6. Since the background scatter is independent of whether the ion is bright

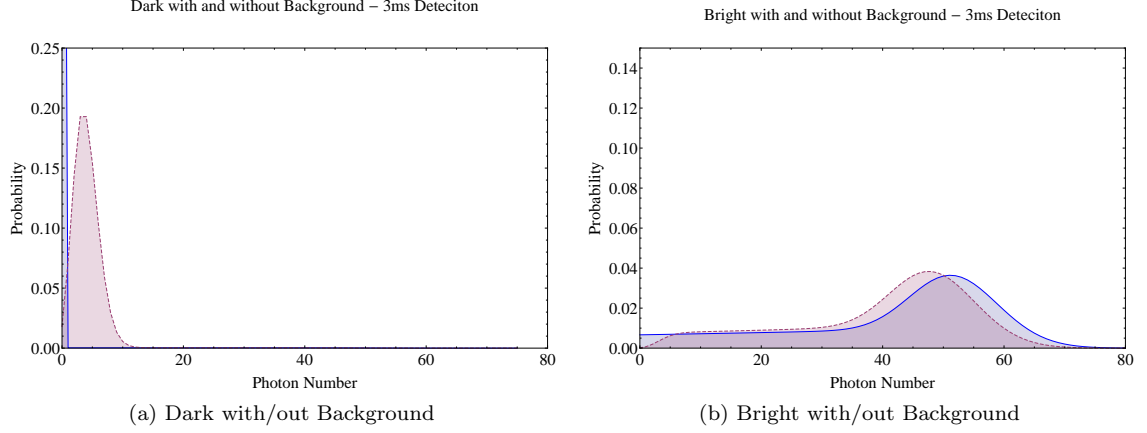


Figure 4.1: Photon Distributions for Bright and Dark Ions with/out Background Scatter. Figure 4.1b shows one bright ion with and without the inclusion of background scatter for a 3ms detection time. Figure 4.1a is the same with a dark ion. The solid blue plot is without the background scatter convolution, whereas the dashed red plot includes the background scatter for both figures. Notice how the distributions are forced out from the zero bin and their shape is changed.

or dark, the photon distribution will be the convolution of the dark or bright distributions with the background scatter. The background scatter takes the form of a Poissonian with a mean λ_{bg} :

$$P_{bg}(n) = P_{\lambda_{bg}}(n) = \frac{e^{-\lambda_{bg}} \lambda_{bg}^n}{n!} \quad (4.1)$$

λ_{bg} is found by measuring the background scatter on the PMT for a given detection time. Thus the convolution of 2.7 and 4.1 results in:

$$P_{dark|bg}(n) = \sum_{k=0}^n P_{dark}(k) P_{bg}(n-k) \quad (4.2)$$

Further, the convolution of 2.6 and 4.1 is:

$$P_{bright|bg}(n) = \sum_{k=0}^n P_{bright}(k) P_{bg}(n-k) \quad (4.3)$$

Equations 4.2 and 4.3 calculate the probability of measuring n photons summing together all possible ways of getting n photons. In Figure 4.1 are plots showing how the distributions are changed with the convolution of the background. As the detection time increases, λ_{bg} increases linearly, shifting both $P_{bright|bg}$ and $P_{dark|bg}$

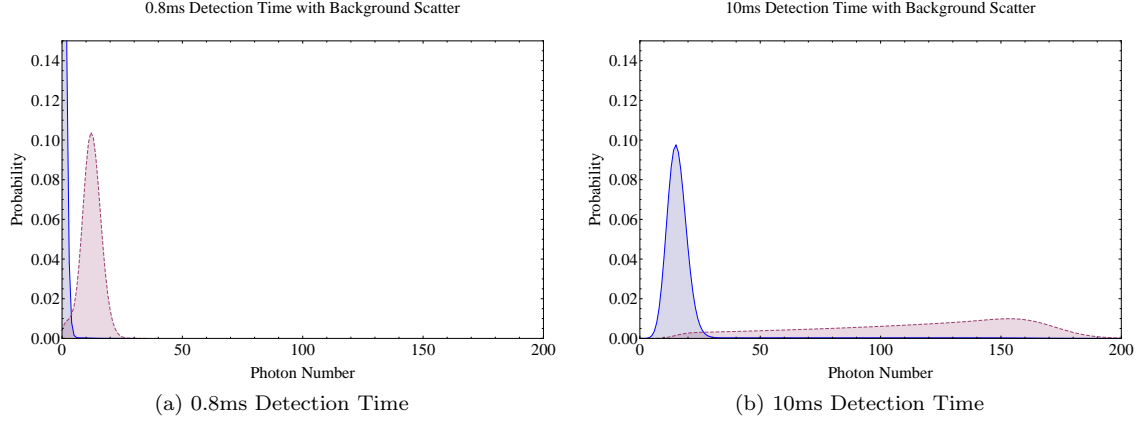


Figure 4.2: Photon Distributions for Multiple Detection Times with Background. Figure 4.2a has the dark and bright photon distributions for one ion with a 0.8ms detection cycle convolved with the background counts. Figure 4.2b is the same, but with a 10ms detection time instead. Notice that the dark and bright counts are forced out from the 0 bin.

over as is exhibited in Figure 4.2. Short detection times, < 1 ms, decrease the overlap of the bright and dark state. Once the detection time is greater than 1ms, the overlap begins to increase again due to the dark histogram moving out from the zero bin. A plot of overlap vs. detection time can be seen in Figure 4.3. This figure shows a minimum overlap of 4% for a detection time of 0.7 ms. This overlap is essentially the probability that a single measurement can be misdiagnosed. This number becomes relevant to us with the camera as this puts a lower limit on our single-shot state detection error. From this calculation, the optimal detection time would be 0.7 ms. At the same time, the small signal size limits the camera detection time. For the camera, the signal must be large enough and spatially focused enough to be distinguishable from the background fluctuations of the CCD. So, there is a lower limit on the detection time. The plot of state detection error vs detection time in Figure 4.4, shows a definite minimum state detection error from 1ms to 7ms, with some local fluctuations. Even though a 1ms detection time seems to give a good state detection error, the separation in the histograms is still small enough that slow, slight fluctuations in the system might cause that error to change. From this data, it

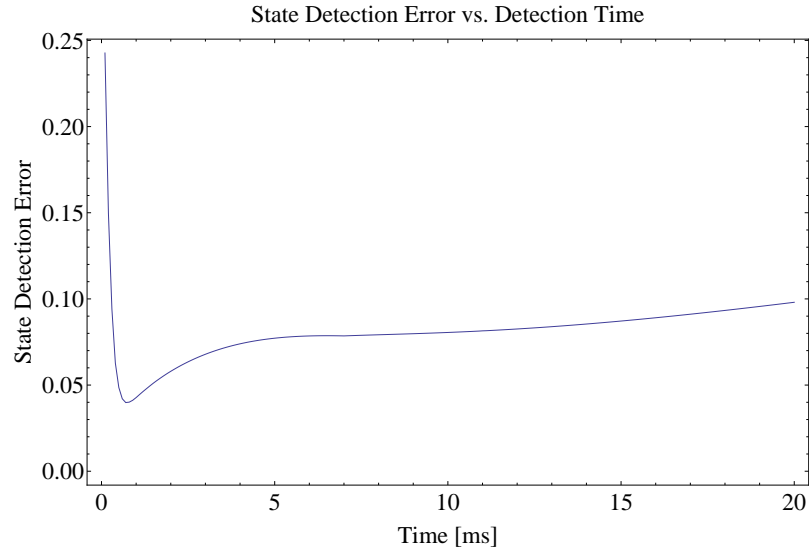


Figure 4.3: Theoretical State Detection Error vs. Detection Time. A theoretical plot of the overlap between the dark and bright state distributions versus detection time. For small detection times, the overlap is significant, but quickly falls off for a minimum around 0.7ms. For longer detection times, the overlap begins to increase again.

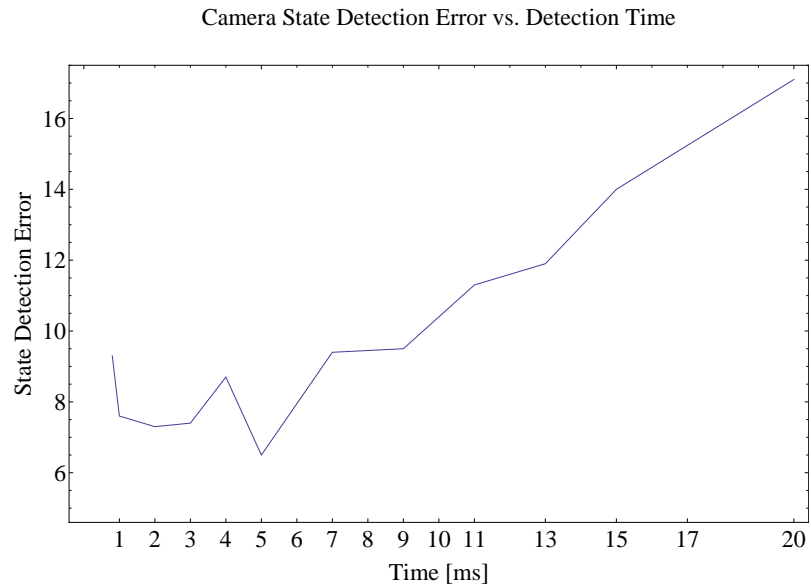


Figure 4.4: State Detection Error with Camera vs. Detection Time. Above is the measured state detection error for selection of detection times. For short times, there is not enough signal to separate the dark from bright state. Increasing the detection time improves state detection until 7 or 8ms. After this, there is a definite trend of increasing error.

appears that the best detection time would be 3ms since this gives the best rep-rate, state detection error, and histogram separation.

4.1.2 Hardware Binning There are a few different ways that the CCD can be “read out”. For this particular camera, the readout is an interline, dual-port readout. Thus, after the camera is exposed, the accumulated charge on the pixels are shifted to a set of pixels that have been masked so they are not sensitive to the light. These interline pixels then move the charge down, one by one, pixel to pixel, to a shift register. This shift register then moves each pixel worth of charge into a pre-amplifier and an analog to digital converter.

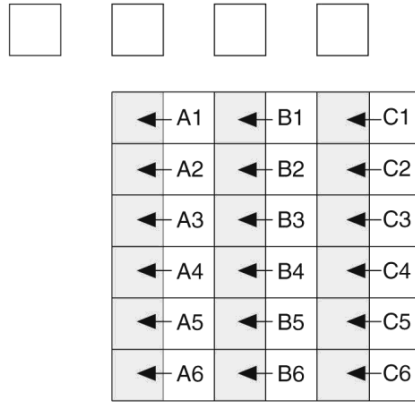
Hardware binning is when the charge from one row is collected with other rows in the shift register before they are digitized and when the shift register collects more than one register pixel into the ADC before digitizing the charge or some combination of the two. Effectively, each individual pixel is collected with the neighboring pixels to form what are called super-pixels.

The benefits of hardware binning are two-fold: better signal to noise ratio and faster readout times. The readout time can be calculated from the equation:

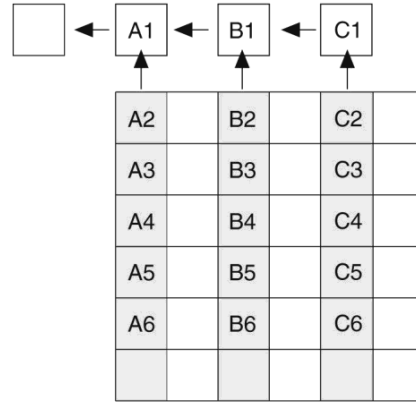
$$t_R = (N_x \times N_y \times (t_{sr} + t_v)) + (N_y \times t_i) \quad (4.4)$$

where N_x is the number of horizontal super-pixels, N_y is the number of the vertical super-pixels, t_{sr} is the time required to shift one pixel of the shift register, t_v is the time required to digitize one pixel, and t_i is the time to shift one line into the shift register. When a region of interest or ROI is selected, namely a piece of the full CCD, this equation can then be applied to the number of pixels in the ROI plus some unavoidable overhead required to dump the unwanted rows. Readout time decreases dramatically as the binning size increases. For example, the readout time of the full CCD goes from 40ms with no binning to 11ms with 4x4 binning. Thus by

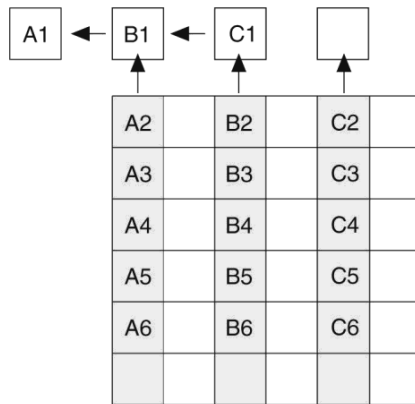
1 Empty Readout Register. Exposure has ended and image is being transferred to storage cells.



2 Image has been shifted to storage cells and first line has been shifted to Readout Register.



3 Charge from first cell has been shifted to the Output Node.



4 After first image are read out, storage cells are empty. Second exposure begins if in Freerun mode. Otherwise, waits for Ext Sync.

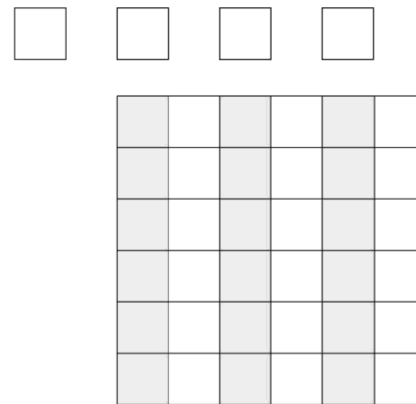
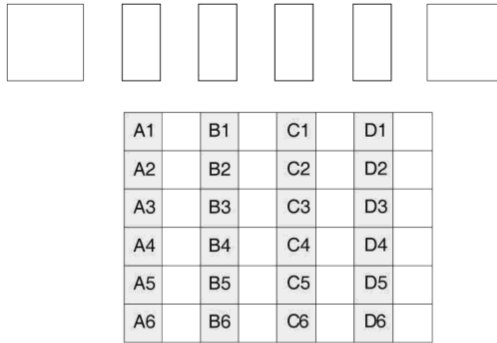
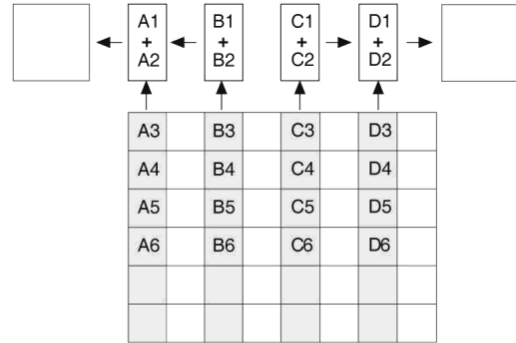


Figure 4.5: Interline CCD Readout Diagram. Courtesy of Princeton Instruments

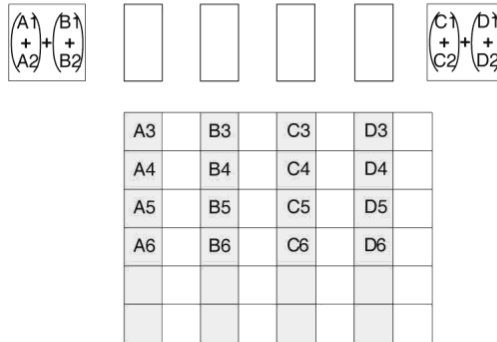
1 Empty Readout Register. Exposure has ended and image has been shifted to storage cells



2 Charges from two storage cells in each column have been shifted to Readout Register and added.



3 Four charges have been shifted to the Output Nodes and added.



4 After sum of first four charges have been transferred from Output Nodes, next set of charges are shifted into Readout Register and added.

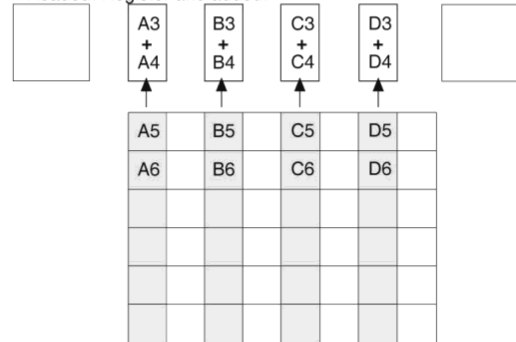


Figure 4.6: 2x2 Binning Diagram. Courtesy of Princeton Instruments

binning, we can improve the rep rate of the experiment to about 100Hz. This greatly improves the number of experiments we can perform before the ion chain melts.

In the regime of small signals which are readout noise limited, binning improves the signal to noise linearly with the number of pixels binned. This is important to our system, since with a 3ms detection time, the mean number of photons collected for a bright ion is only 45. By binning, we are able to increase our signal beyond the readout noise, whereas without it, they are almost the same.

In general, the readout noise of the camera is a non-linear function relative the binning size. In order to find out the magnitude of the readout noise, we first blocked all light from the camera and took 1000 shots for different binning values. The CCD rms shot noise when light is present is: $g\sqrt{N}$ where g is a large gain factor and N is the number of incident photons. And so, when light is incident on the CCD, the signal-to-noise ratio has the form:

$$S/N = \frac{gN}{\sqrt{g^2N + d_c^2 + m\sigma_r^2}} = \frac{N}{\sqrt{N + \frac{d_c^2}{g^2} + \frac{(m\sigma_r)^2}{g^2}}} \quad (4.5)$$

where d_c is the dark current, σ_r is the readout noise, and m is the number of pixels read. Since the camera CCD is kept very cold with a set point of $-25^\circ C$, the dark current noise is very small. Therefore, $\left(\frac{d_c}{g}\right)^2 \approx 0$. Thus, if the camera were to be exposed without any light falling on it, the signal would be zero and so the noise present on the readout pixels would be:

$$Noise = \sqrt{N + \left(\frac{d_c}{g}\right)^2 + \left(\frac{m\sigma_r}{g}\right)^2}$$

As $\left(\frac{d_c}{g}\right)^2, N \Rightarrow 0$

$$Noise \Rightarrow \frac{m\sigma_r}{g}$$

If the consideration were to be limited to only one pixel, then the only noise present

Table 4.1: Binning Noise Analysis 3ms DT

Binning	σ_r/g	S/N
1x1	33	1.3
2x2	59	4.0
4x4	71	5.2
8x8	147	5.5
16x16	291	5.5
32x32	490	4.5
64x64	1100	6.0

on the CCD would be the effective readout noise and so the standard deviation of the pixel value would then be equal to this readout noise. Using this method, we found the readout noise for the binnings to be as marked in Table 4.1. While the readout noise begins to increase with the binning size, the signal-to-noise ratio is also increasing due to the fact that as the binning increases, the ADC error has a non-linear form which does not increase rapidly. Effectively, increasing the binning size decreases the number of ADC operations which improves the signal-to-noise ratio. In order to find the best binning for our experiment, we analyzed a bright ion at different binning values. Upon examination of the histograms of a bright ion vs. a dark ion for the different binnings, clearly binning improves the discrimination between the two histograms. The plot in Figure 4.7 confirms that state detection improves as binning size increases. From this data, the larger binning appears to improve our fidelity. Yet, there is a limit on the binning due to the separation of the ions. If the super-pixels are the same size as the separation of the ions, then the cross-talk discussed in Chapter III overwhelms the dark ion signal. For example, the effective pixel size with an 8x8 binning is $102 \times 102 \mu m$. If the ion spot size at the CCD is $247 \mu m$, then the best possible situation is where the ion signal is spread over a minimum of three super-pixels, making the ion size in the data effectively $306 \mu m$. This greatly increases the amount of crosstalk for large numbers of ions. If the binning is only divided in

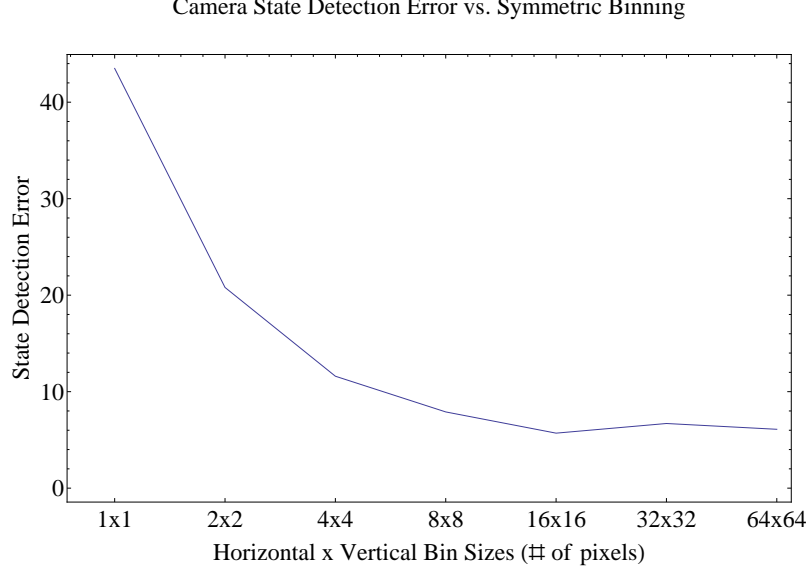


Figure 4.7: State Detection Error with Camera vs. Hardware Binning. Above is the measured state detection error for increasing symmetric binning sizes. For small binnings, the detection error is very large. Increasing the number of pixels that are included in a super-pixel significantly decreases this error.

Table 4.2: Asymmetric Binning Noise Analysis 3ms DT

Binning	σ_r/g	S/N
4x8	77	5.0
4x16	84	4.8
4x32	97	6.6
4x64	120	6.2
4x128	160	6.5

half, the effective size of the ion goes down to $256\mu m$. Crosstalk then limits the binning to 4 pixels in the horizontal direction. This constraint does not effect the vertical direction since the image of the ion chain is oriented horizontally on the camera. The PI-Max3 1024i camera is capable of asymmetric binning. Thus the signal-to-noise can be increased by binning in the vertical direction without affecting the crosstalk. Figure 4.8 shows definite improvement over the symmetric binning 4x4, and the error further reduces as the vertical binning increases. Due to the improvement in readout times for larger binnings, the best binning size is the largest one possible. The only limitation might be that the binning should not be so large

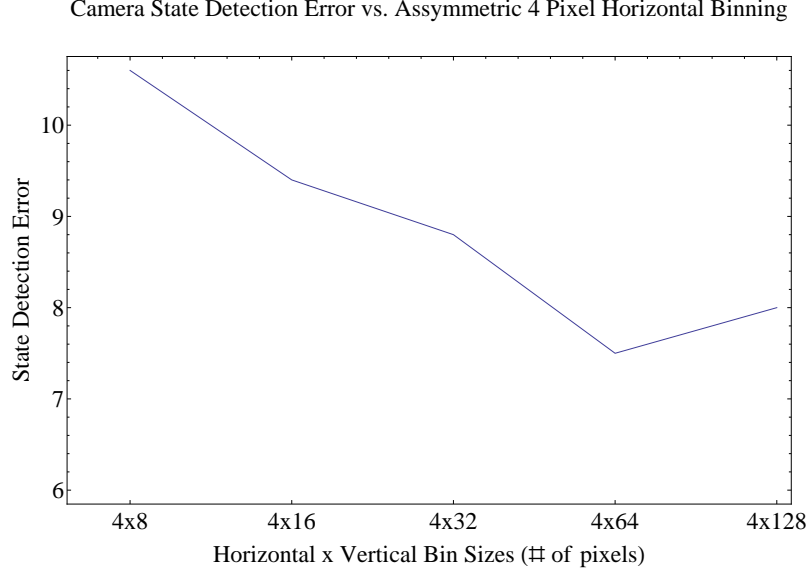


Figure 4.8: State Detection Error with Camera vs. Asymmetric Hardware Binning. Here is a comparison of the state detection error to asymmetric binning sizes where the horizontal binning size has been fixed at 4.

as to include many more pixels than the size of the ion in the vertical direction to reduce scatter noise.

4.2 Camera Data Analysis

Once the best camera settings have been chosen, there is still a difficulty in deciding whether the ion is bright or not. The first difficulty is deciding which super-pixels are considered to be the signal from a given ion. The next difficulty is deciding whether the ion is bright or dark for a given detection period. Both of these problems will contribute to error in the state detection. We explored several methods of data analysis in order to determine which gave us the best state detection.

4.2.1 Box-Sum Method The Box-Sum Method is as simple as the name suggests. Each ion has a box on the CCD designated to be its signal and that box is summed to determine whether the ion is bright or dark. The real crux of this method is appropriately determining the box and choosing the threshold for where the ion

is dark or bright. In order to fully flesh out the probability distribution, we first initialize the ions into the $|\downarrow\rangle$ via optical pumping and then detect. We repeat this for a large number of times (typically 1000). We then do the same with the $|\uparrow\rangle$. Then each set of data is averaged and the dark average is subtracted from the bright average. This is then the average signal from all of the ions. The average signal is then filtered such that all values below a certain level are set to zero (typically 40% the maximum value). The resulting image contains only the most significant light from each ion. For each ion, a box region of pixels is then determined that maximally covers the signal while minimizing the number of pixels selected.

Once the boxes have been selected, the ion region values are totaled for each of dark shots and bright shots. These values are collected together into a histogram. In order to prevent the dark state from being preferred over the bright state, a threshold must be selected such that the error for the selection of the dark state is the same as that for the selection of the bright state. To accomplish this, the threshold is chosen by finding the point where the dark and bright histograms have the same number of counts on the wrong side of the threshold. The state detection error is then calculated by dividing the average number of shots which were misidentified between dark and bright by the total number of shots taken.

This method works well for the analysis for a few ions in the trap due to its simplicity and speed. State discrimination can be performed in real time without slowing down the rep-rate of the experiment. The difficulty with this method is its susceptibility to crosstalk. Since the box-sum method neglects any information that might be present between the ions, any photons that fall on the box region contribute purely to the brightness of that ion. In order to quantify how much each ion is contributing to its neighbors, we first took 1000 shots of bright and dark states

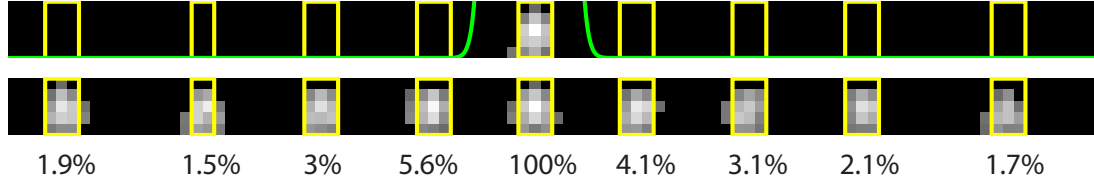


Figure 4.9: Signal Contribution of Ions to Other Positions. The top part of the figure pictures 1 ion with the box positions of the 9 ion image below. Beneath is the averaged signal values of the 1 ion run at each of the 9 ion positions in terms of a percentage of the central value. The green is a portion of the Gaussian fit to the ion signal on the CCD, showing the width of the signal on the CCD.

for 1, 3, 5, and 9 ions with a fixed axial voltage setting. We chose an odd number of ions so that the center ion would be at the same position for each data set. Then we found the box size and positions for each of the multi ion data sets. These boxes were then applied to the 1 ion data set and the values of each box were then compared. If the data is taken with a binning width of 8 pixels, then the contribution to the nearest neighbor is about 12% of the ion signal. If the binning width is reduced to 4 pixels, this is cut in half to 5.6%. This can be explained as the effective spot size of the ion increases from $250\mu m$ to $300\mu m$ on the CCD when the binning is increased from 4 pixel binning in the horizontal direction to 8 pixel binning, the amount of signal overlap also increases.

4.2.2 Gaussian Fit Method: 1-D The Gaussian 1-D Fit method is a slightly more complicated approach to discriminating a dark ion from bright. In this case, the entire region of interest is summed down to a single row. This means that all of the pixel values in the vertical direction are summed down so that only the horizontal dimension remains. This single row is essentially a cross-section of the region of interest. We use the vertical sum instead of just one row in the middle because the ion signal is still much larger than the background, since the S/N ratio of each pixel

is large for a binned super-pixel. More image contrast is gained by using the sum than not. Once the region has been reduced to a single row, a sum of Gaussian distributions are fit to the row, where there is a distribution for each ion. The amplitude of the distribution is then discriminated in a similar way to the sums of the box-sum method in order to discern whether the ion is bright or dark.

The calibration of the Gaussian distributions then replaces the determination of the box size, but is accomplished in a similar manner. The ions are all pumped bright and dark for a large number of shots each. The bright shots are averaged and the dark shots are subtracted from the bright to leave just the signal. This averaged signal is then reduced to a single row where the maxima are found. These maxima are used as the centers of the Gaussian distributions. A sum of Gaussians for the number of ions is then formed and fit to the averaged signal to find the width of each ion:

$$\sum_{i=1}^N A_i e^{-\frac{(x-x_i)^2}{w_i^2}} + O \quad (4.6)$$

where N is the total number of ions, i is the ion index, A_i is the ion signal amplitude, x_i is the ion center, w_i is the width of the ion's distribution and O is a constant offset. The centers and width are then used to form a final sum where the only free parameter is the amplitude of each term and an offset term, since a “dark” pixel has some value. The final sum of Gaussian distributions is then applied individually to each of the bright and dark shots and the histograms are compared in the same way as the box-sum method. This results in an error and a threshold for each Gaussian, determining what amplitudes are bright or dark.

Once the calibration has taken place, every data point is then reduced to a single row and the final Gaussian sum is applied to each data point and each ion is discriminated as bright or dark according to the found threshold. The benefit to this method

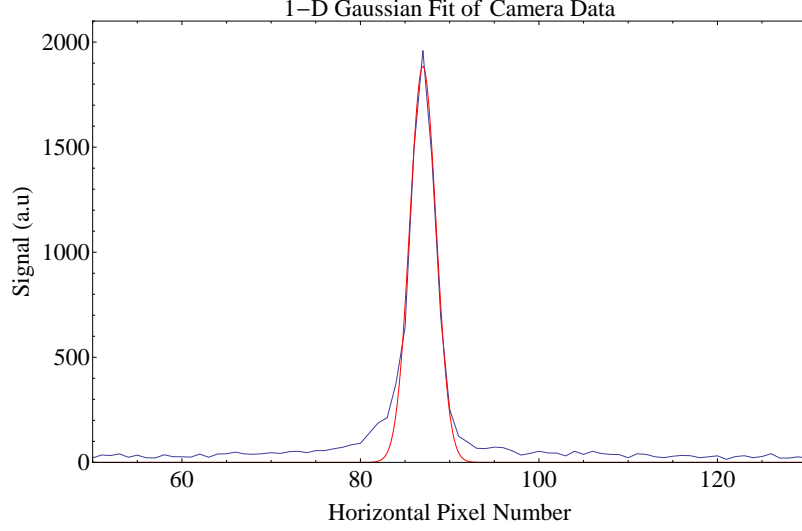


Figure 4.10: Summed Single Row Data and 1-D Gaussian Fit. Here is an example of a Gaussian fit to the vertically summed data. Since the distribution takes into account the overlap with the neighboring ions, the effect of crosstalk is diminished.

is that more information is taken into account by the distribution since the fit makes use of the data between the ion signals. Thus, the effect is crosstalk is minimized since the fitting already takes the signal overlap into account. The fitting cannot compensate for crosstalk perfectly, since the actual distribution on the CCD is an Airy ring and the Gaussian is just an approximation. The ability of the Gaussian fit to better neglect crosstalk is evidenced by the fact that when the horizontal binning is 8 pixels, while the box-sum method results in a nearest neighbor contribution of 12%, the fitting method has a value of 6%. When the horizontal binning is set to 4 pixels, this value goes down to 5.3%. For the 4 pixel binning width, the box-sum method and the Gaussian 1-D fit are equivalent.

4.2.3 Gaussian Fit Method: 2-D A similar method can be applied to the entire region of interest, not just a 1-D summed row. Now the sum of Gaussians takes the form:

$$\sum_{i=1}^N A_i e^{-\left(\frac{(x-x_i)^2}{w_{x_i}^2} + \frac{(y-y_i)^2}{w_{y_i}^2}\right)} + O \quad (4.7)$$

where y_i is the vertical center and w_{y_i} is the vertical width. At first glance, it appears that using more spatial information should improve the resiliency to crosstalk. This is not the case, since the high vertical binning value makes any 2-D fit very poor and hard to discriminate. Since the S/N ratio goes down as the vertical binning is reduced, the 2-D Gaussian fit ends up losing more discrimination than it gains. This, when compounded with the fact that the readout time is slower and that the amount of memory required is increased, means that it is better to use just a 1-D fit to the summed horizontal row.

4.2.4 Inverted State Matrix The inherent difficulty with any method which fits to the camera image is that each individual shot will not have enough photons to sufficiently produce a distribution. For this reason, we explored a method which is essentially a modification of the box-sum method. First, we fit the 1-D Gaussians to the single row data and extract the parameters for each fit (the width and location of the distribution). Then, for each individual Gaussian, we integrate the Gaussian at each ion location, which is defined by the ions center and its width. Thus for ion i , we find a box such that $(x_i - w_i, x_i + w_i)$ is the ion region. The integration of the Gaussian for each ion over every ion region produces an $N \times N$ matrix, where N is the total number of ions. This matrix represents the amount of signal spill-over from each ion at the other ion locations. If the matrix is formed such that each row represents the signal contributions at a single ion location from every ion, then by multiplying this matrix by the “perfect” state vector, we would extract our measured values.

$$\begin{pmatrix} M_1 \\ M_2 \\ M_3 \\ \vdots \end{pmatrix} = \begin{pmatrix} C_{1,1} & C_{2,1} & C_{3,1} & \cdots \\ C_{1,2} & C_{2,2} & C_{3,2} & \cdots \\ C_{1,3} & C_{2,3} & C_{3,3} & \cdots \\ \vdots & \vdots & \vdots & \ddots \end{pmatrix} \begin{pmatrix} I_1 \\ I_2 \\ I_3 \\ \vdots \end{pmatrix} \quad (4.8)$$

Here M_1, M_2 , etc. represent the actual measured values, $C_{m,n}$ represents the contribution of ion m at ion location n , and I_1, I_2 , etc. represents the perfect signal of the ion without crosstalk. Thus, by inverting this state matrix, we can extract the ideal signal from the measured signal. By calibrating with a large number bright ion shots and a large number of dark ion shots in the same way as the box-sum and 1-D Gaussian fit, we can find a threshold for the ideal values that best distinguishes the dark ion from the bright ion.

Using this method, we found that while the state matrix inversion did well in suppressing the crosstalk to the other ions, it was extremely susceptible to variations in the background counts. These variations may arise from many different sources (changing laser intensity, camera offset fluctuations, etc.). Thus, even though the state matrix inversion was slightly better at suppressing crosstalk, the Gaussian fit method has overall better resiliency against slow fluctuations in the system.

4.3 Crosstalk Analysis

In prior sections, the subject of ion signal crosstalk has been addressed, but not been resolved. This error is a difficult value to measure, since the best measure would be to have a single dark ion surrounded by a large number of bright ions. With the current experimental setup, we are unable to prepare a state like this since it would require the ability to individually address an ion, whereas our system currently uses global beams. Thus, some other method of extracting the crosstalk is required. One

Average 9 Ion Correlation with Three Methods

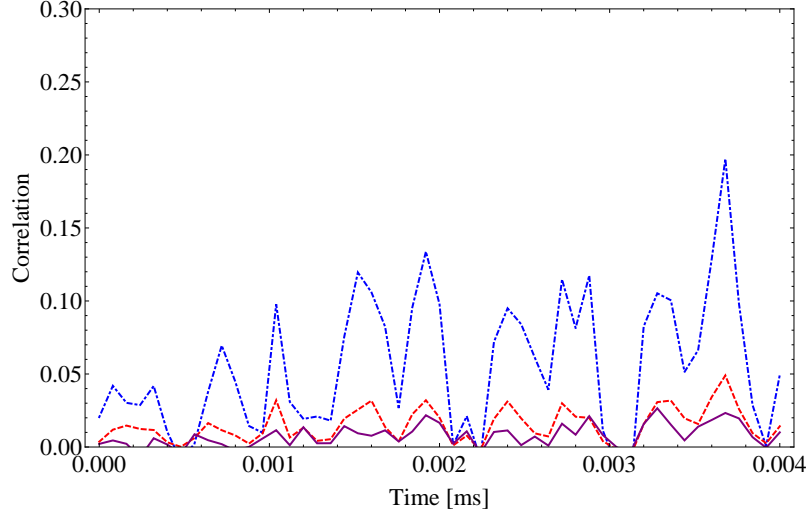


Figure 4.11: Average Value of Correlation Function along Ion Chain. This is an average of the correlation function, $C_{i,j}$, across the ion chain of 9 ions. The spikes in the function occur at multiples of $\Omega_{Rabi}t = \frac{\pi}{2}$, since these times have a high probability of having a bright ion adjacent to a dark ion.

method is to use a correlation function. A correlation function in general is the correlation between random variables at two different points in space or time. In our case, the correlation function will be looking at the correlation between ion measurements as a function of ion position. We define the function as follows:

$$C_{i,j} \equiv \langle \sigma_i \sigma_j \rangle - \langle \sigma_i \rangle \langle \sigma_j \rangle \quad (4.9)$$

where i and j are the ion position indices and $\langle \sigma_i \rangle$ is the expectation value of the spin at the i th position. This correlation function is zero as long as there is no dependence of the spins on each other, since the expectation value of the product should equal the product of the expectation values when the spins are independent. The function is therefore non-zero only when there is some entanglement between the two ions or when there is signal spillover. In order to measure the amount of crosstalk, we took a large string of ions (9 or 10 ions) and simply pumped them with the Raman beams for increasing lengths of time so that they would perform Rabi oscillations. Thus each ion

was oscillating between bright and dark but since there was no interaction between the ions, there was no entanglement and the signals were independent of each other. We then applied this correlation function to the discriminated ion signals from both the box-sum method, the Gaussian 1-D fit method, and the state matrix inversion method. The average plot of $C_{i,j}$ vs time can be seen in the Figure 4.11. As is demonstrated in the figure, the box-sum method has a greater sensitivity to crosstalk than the fit method, while the state matrix inversion has the least sensitivity. The crosstalk, unsurprisingly, is not uniform across the ion chain. There is an increase in the correlation function when looking at ions 4 and 5 as compared to ions 1 and 2 (See Figure 4.12), which makes sense since the ions at the center of the chain end up being closer together than the ions at the ends. In order to quantify the crosstalk in general, we took the average of the correlation function across the ion chain and over the duration of the measurement. The final result was:

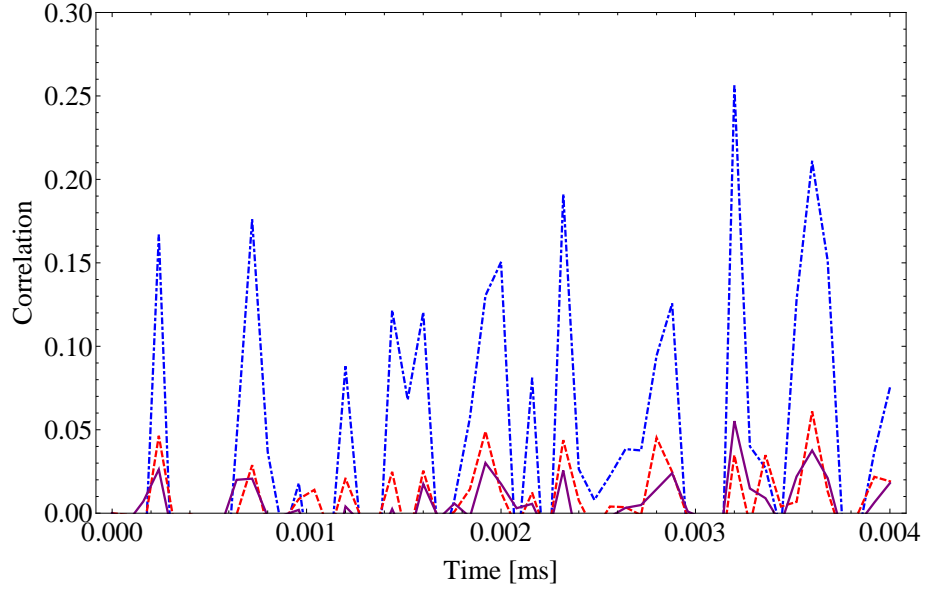
$$\sigma_{box} = 5.5\%$$

$$\sigma_{fit} = 1.5\%$$

$$\sigma_{matrix} = 0.8\%$$

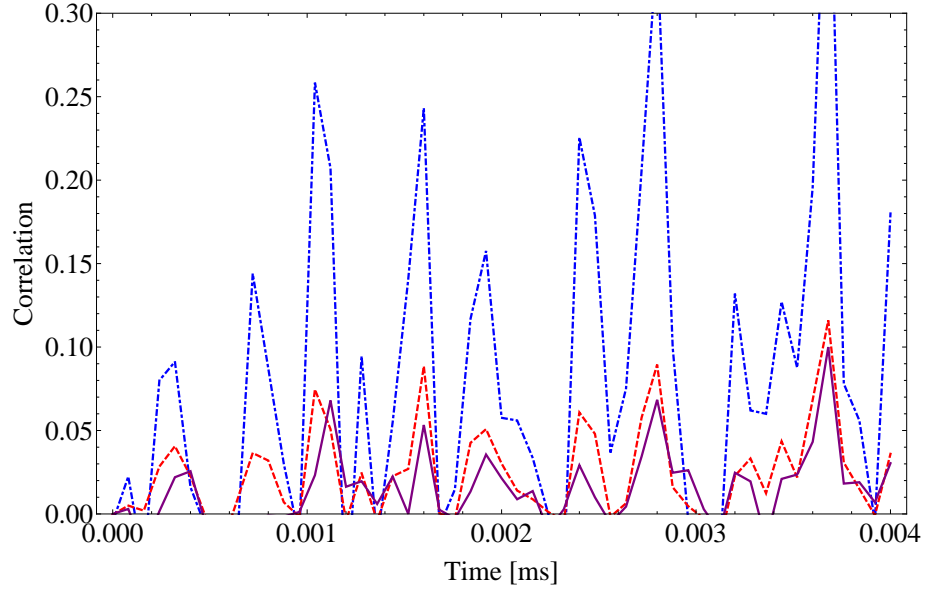
where σ_{box} is the error due to crosstalk with the box-sum method, σ_{fit} with the Gaussian 1-D fit method, and σ_{matrix} with the state matrix inversion method.

Correlation of Ion #1 and #2 in 9 Ion Chain with Two Methods



(a) Correlation of Ions #1 and #2

Correlation of Ion #4 and #5 in 9 Ion Chain with Two Methods



(b) Correlation of Ions #4 and #5

Figure 4.12: Correlation Function Values for Different Positions on Ion Chain. Figure 4.12a is a plot of the correlation function of all three methods of data analysis for the first two ions, #1 and #2. The same is plotted for the ions in the middle of the chain, ion #4 and #5, in Figure 4.12b. In both Figures 4.12a and 4.12b, the dotted blue line corresponds to the box-sum method and the red dashed line corresponds to the 1-D Gaussian fit and the solid purple line corresponds to the state matrix inversion

CHAPTER V

Final Results and Conclusion

5.1 Final Results

The conclusion we take from Chapter IV is that the camera yields the best results if we use a detection time of 3ms and an asymmetric binning of 4x64. These settings should yield a state detection error of:

$$\sigma_{camera} = 5\% \tag{5.1}$$

This final state detection error is actually lower than theoretical detection fidelity discussed in section 4.1.1 due to the overlap of the bright state with the dark state for a 3ms detection time. The discrepancy can be explained by the fact that the calculated distribution was found for all detected photons, but due to the spatial resolution of the camera, some of the background scatter on the CCD is ignored.

In order to quantify this final state detection error in comparison with the PMT, we performed a similar analysis on the PMT. Just as with the camera, we prepared the ion bright and dark for a large number of experiments, in this case 1000. We then formed a histogram of all the photon counts from the PMT and found the bin where error was the same for both bright and dark. From this, we calculated the error of the PMT:

$$\sigma_{PMT} = 3\% \tag{5.2}$$

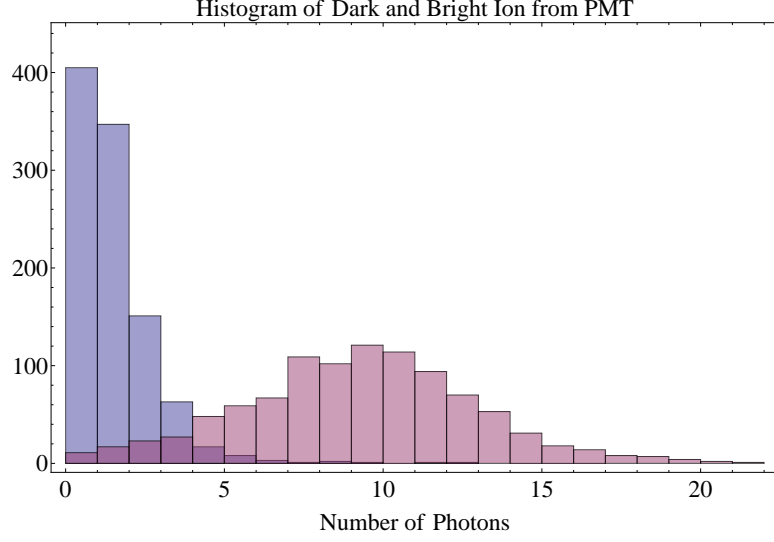


Figure 5.1: PMT Histogram of Dark and Bright Ion. This a comparison of the dark and bright histograms on the PMT for a detection time of $0.8ms$.

The histogram can be seen in Figure 5.1.

In addition to the stated σ_{camera} , there is a state detection error due to crosstalk from the other ions. This error is dependent on the number of ions and the state of the ions. When the ions are all dark or all bright, there is very little contribution of the crosstalk to the state detection error. When the ions are in a state where half are bright, half are dark, the crosstalk contributes to the state detection error. In this worst case scenario, the total detection error will be:

$$\begin{aligned}\sigma_{total} &= \sqrt{\sigma_{camera}^2 + \sigma_{fit}^2} \\ &= 5.2\%\end{aligned}$$

where $\sigma_{camera} = 5\%$ and $\sigma_{fit} = 1.5\%$ is assumed based on the σ_{fit} found as the average crosstalk found in section 4.3. At worst, crosstalk from other ions only contributes 0.2% to the state detection error when the states are analyzed using a 1-D Gaussian fit. If instead the ion states were analyzed with the box-sum method,

the total error would be:

$$\begin{aligned}\sigma_{total} &= \sqrt{\sigma_{camera}^2 + \sigma_{box}^2} \\ &= 7.4\%\end{aligned}$$

Clearly the Gaussian fit improves our state discrimination significantly.

Therefore, the best possible state discrimination error which can be achieved is $\sigma = 5.2\%$. Of course, due to fluctuations in laser power and/or beam alignment, this number fluctuates in actual working conditions, requiring the calibration of the camera prior to taking data. These fluctuations typically only result in a deviation of $\pm 1\%$.

While the PMT still has better state discrimination for one ion and readout speed, the benefits of the camera still outweigh the drawbacks. With the camera, we can now watch each ion evolve individually during our experiment. A plot of 9 ions Rabi flopping is shown in Figure 5.2, where each ion is a different plot. In this case, the ion chain can be seen to have unequal illumination from the Raman beams, resulting in a different Rabi frequency for each ion.

5.2 Conclusion

In conclusion, the Princeton Instruments PIMax3: 1024i ICCD camera is a significant step forward for our experiment as it offers spatial discrimination and single shot measurement. There is still room for improvement, however, since the single shot state discrimination of the entire chain of 10 ions is still limited to only 60%.

There are still some possible methods of detection that might lead to better state discrimination. For example, instead of using an ICCD with 1024x1024 pixels, which has far greater resolution than we need, we might instead use an intensifier, which would transform the 369 nm light into a greater number of green photons, and

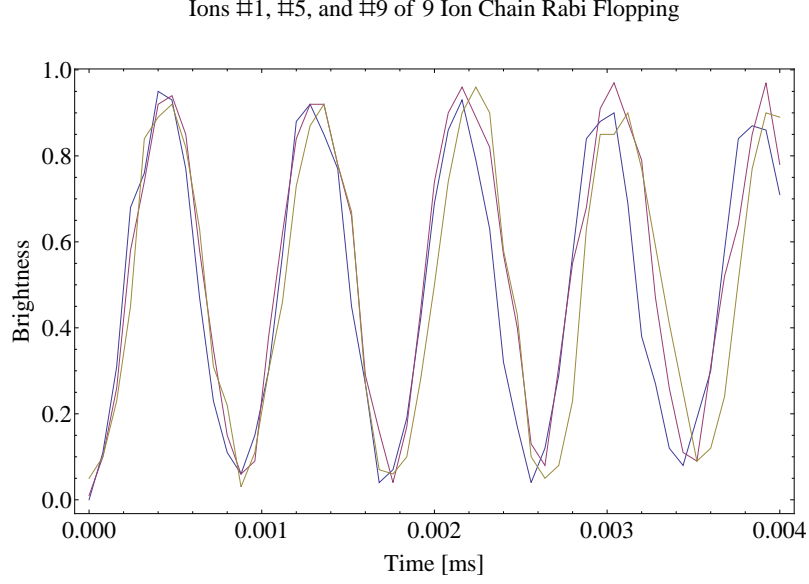


Figure 5.2: Many Ion Rabi Flopping. Above is a plot of ion numbers 1, 3, and 9 of a nine ion chain performing $4.5 \, 2\pi$ rotations or “flops”. The detection apparatus used was the PIMax3:1024i camera. Due to a slight misalignment of the Raman beams, ion #9 is rotating slightly slower than ion #1. Such observations were not possible on the PMT due to the lack of spatial discrimination.

image the result onto an array of PMTs such that the required resolution could be reproduced. The benefits of this method would be the state detection and speed of a PMT with the spatial discrimination of the camera. The drawback is that such a device is still theoretical and any implementation would yield unforeseen and potentially prohibitive difficulties.

Another means of improving state detection would be to “shelve” the dark state. Shelving would involve pumping the dark ions into some other state far detuned from the bright state. Detection would then consist of light resonant with the bright transition and also light resonant with the $|\downarrow\rangle$ to the ${}^2P_{1/2} |F = 1\rangle$ transition, which couples back to the bright transition. The only theoretical limitation on the detection fidelity would be the fidelity of the coupling of the dark state to the shelving state, since we would no longer have to selectively excite the hyperfine sub-manifold, but could blast the entire ${}^2P_{1/2}$ state during detection. Considering that this theoretical

shelving state would have to couple poorly or not at all to the dark state, shelving the ion might be as bad as or even worse than the current state detection.

While there is room for a better detection system, the amount of physics available to us with the camera is still vast. With only PMT detection, we were not able to study dynamic systems. The ICCD camera enables us to study the dynamics of small quantum systems. Better understanding of these small systems will enable us to improve our comprehension of larger system dynamics and will yield real world ramifications.

BIBLIOGRAPHY

BIBLIOGRAPHY

- [1] R. Feynman, “Simulating Physics with Computers”, *International Journal of Theoretical Physics* **21**, 467 (1982).
- [2] S. Lloyd, “Universal Quantum Simulators”, *Science* **273**, 1073 (1996).
- [3] D. P. DiVincenzo, “The Physical Implementation of Quantum Computation”, *Fortschritte der Physik* **48**, 771 (2000).
- [4] R. Moessner and A. P. Ramirez, “Geometrical Frustration”, *Physics Today* **59**, 24 (2006).
- [5] K. Binder and A. P. Young, “Spin glasses: Experimental facts, theoretical concepts, and open questions”, *Rev. Mod. Phys.* **58**, 801 (1986).
- [6] L. Balents, “Spin liquids in frustrated magnets”, *Nature* **464**, 199 (2010).
- [7] T. Moriya and K. Ueda, “Antiferromagnetic spin fluctuation and superconductivity”, *Reports on Progress in Physics* **66**, 1299 (2003).
- [8] S. Sachdev, “*Colloquium*: Order and quantum phase transitions in the cuprate superconductors”, *Rev. Mod. Phys.* **75**, 913 (2003).
- [9] F. Barahona, “On the computational complexity of Ising spin glass models”, *Journal of Physics A: Mathematical and General* **15**, 3241 (1982).
- [10] B. A. Cipra, “The Ising Model Is NP-Complete”, *SIAM News* **33** (2011).
- [11] E. Farhi et al., “A Quantum Adiabatic Evolution Algorithm Applied to Random Instances of an NP-Complete Problem”, *Science* **292**, 472 (2001).
- [12] S. Lloyd, “Quantum Information Matters”, *Science* **319**, 1209 (2008).
- [13] I. Buluta and F. Nori, “Quantum Simulators”, *Science* **326**, 108 (2009).
- [14] J. J. Garcia-Ripoll, E. Solano, and M. A. Martin-Delgado, “Quantum simulation of Anderson and Kondo lattices with superconducting qubits”, *Phys. Rev. B* **77**, 024522 (2008).
- [15] E. J. Pritchett et al., “Quantum Simulation of Molecular Collisions with Superconducting Qubits”, *quant-ph*, 1008.0701 (2010).
- [16] T. Byrnes, N. Y. Kim, K. Kusudo, and Y. Yamamoto, “Quantum simulation of Fermi-Hubbard models in semiconductor quantum-dot arrays”, *Phys. Rev. B* **78**, 075320 (2008).
- [17] M. Lewenstein et al., “Ultracold atomic gases in optical lattices: mimicking condensed matter physics and beyond”, *Adv. Phys.* **56**, 243 (2007).
- [18] S. Trotzky et al., “Time-resolved observation and control of superexchange interactions with ultracold atoms in optical lattices”, *Science* **319**, 295 (2008).

- [19] G.-B. Jo et al., “Itinerant Ferromagnetism in a Fermi Gas of Ultracold Atoms”, *Science* **325**, 1521 (2009).
- [20] T. A. Corcovilos, S. K. Baur, J. M. Hitchcock, E. J. Mueller, and R. G. Hulet, “Detecting antiferromagnetism of atoms in an optical lattice via optical Bragg scattering”, *Phys. Rev. A* **81**, 013415 (2010).
- [21] J. Simon et al., “Quantum Simulation of an Antiferromagnetic Spin Chain in an Optical Lattice”, *cond-mat.quant-gas*, 1103.1372 (2011).
- [22] D. Porras and J. I. Cirac, “Effective Quantum Spin Systems with Trapped Ions”, *Phys. Rev. Lett.* **92**, 207901 (2004).
- [23] X.-L. Deng, D. Porras, and J. I. Cirac, “Effective spin quantum phases in systems of trapped ions”, *Phys. Rev. A* **72**, 063407 (2005).
- [24] L. Lamata, J. León, T. Schätz, and E. Solano, “Dirac Equation and Quantum Relativistic Effects in a Single Trapped Ion”, *Phys. Rev. Lett.* **98**, 253005 (2007).
- [25] M. Johanning, A. F. Varn, and C. Wunderlich, “Quantum simulations with cold trapped ions”, *Journal of Physics B: Atomic, Molecular and Optical Physics* **42**, 154009 (2009).
- [26] A. Friedenauer, H. Schmitz, J. T. Glueckert, D. Porras, and T. Schaetz, “Simulating a quantum magnet with trapped”, *Nature Physics* **4**, 757 (2008).
- [27] K. Kim et al., “Quantum simulation of frustrated Ising spins with trapped ions”, *Nature* **465**, 590 (2010).
- [28] E. E. Edwards et al., “Quantum simulation and phase diagram of the transverse-field Ising model with three atomic spins”, *Phys. Rev. B* **82**, 060412(R) (2010).
- [29] R. Islam et al., “Onset of a Quantum Phase Transition with a Trapped Ion Quantum Simulator”, *quant-ph*, 1103.2400 (2011).
- [30] R. Gerritsma et al., “Quantum simulation of the Dirac equation”, *Nature* **463**, 68 (2010).
- [31] J. T. Barreiro et al., “An open-system quantum simulator with trapped ions”, *Nature* **470**, 486 (2011).
- [32] D. Leibfried, R. Blatt, C. Monroe, and D. Wineland, “Quantum dynamics of single trapped ions”, *Rev. Mod. Phys.* **75**, 281 (2003).
- [33] D. Wineland and R. Blatt, “Entangled states of trapped atomic ions”, *Nature* **453**, 1008 (2008).
- [34] H. Haffner, C. F. Roos, and R. Blatt, “Quantum computing with trapped ions”, *Nature* **453**, 1008 (2008).
- [35] S. Olmschenk et al., “Manipulation and detection of a trapped Yb^+ hyperfine qubit”, *Phys. Rev. A* **76**, 052314 (2007).
- [36] B. King, *Quantum state engineering and information processing with trapped ions*, PhD thesis, University of Colorado, 1999.
- [37] C. F. Roos, *Controlling the quantum state of trapped ions*, PhD thesis, Universität Innsbruck, 2000.
- [38] M. Acton, *Detection and Control of Individual Trapped Ions and Neutral Atoms*, PhD thesis, University of Michigan, 2008.